Contact-free Vital Sign Monitoring Using Phase Difference of Channel State Information

by

Chao Yang

A thesis submitted to the Graduate Faculty of
Auburn University
in partial fulfillment of the
requirements for the Degree of
Master of Science

Auburn, Alabama
Dec 16, 2017

Keywords: WiFi Signal, Phase Measurement, Vital Sign, Channel State Information

Approved by

Shiwen Mao, Samuel Ginn Endowed Professor of Electrical and Computer Engineering
Thaddeus Roppel, Associate Professor of Electrical and Computer Engineering
Yin Sun, Assistant Professor of Electrical and Computer Engineering

Abstract

Vital signs, such as breathing and heartbeat, are useful to health monitoring since such signals provide important clues of medical conditions. Effective solutions are needed to provide contact-free, easy deployment, low-cost, and long-term vital sign monitoring. In this paper, we present PhaseBeat to exploit channel state information (CSI) phase difference data to monitor breathing and heartbeat with commodity WiFi devices. We provide a rigorous analysis of the CSI phase difference data with respect to its stability and periodicity. Based on the analysis, we design and implement the PhaseBeat system with off-the-shelf WiFi devices, and conduct an extensive experimental study to validate its performance. Our experimental results demonstrate the superior performance of PhaseBeat over existing approaches in various indoor environments.

Acknowledgments

Firstly, I am very grateful to my advisor Prof. Shiwen Mao for his guidance. He inspired me a lot whenever I had problem with my research work. I also appreciate my other committee members, Prof. Thaddus Roppel, and Prof. Yin Sun. They gave me lots of suggestions and helpful comment, so that I can modify and improve my thesis research.

Besides these professors, I would like to thank my team members, particularly, Xuyu Wang, who helped me a lot in my research field. I can't make a success in my research and other projects without his help.

Last but no the least, I want to thank my family members and friends, who give support with their love during my whole study in Auburn.

Table of Contents

List of Figures

Chapter 1

Introduction

It is estimated that over 100 million Americans have chronic health conditions, such as lung disorders and heart diseases. Three-fourths of the total US healthcare cost are spent to treat these conditions [1], leading to an increasing demand for long-term health monitoring in indoor environments. Vital signs, such as breathing and heartbeat, are useful to physical health monitoring since such signals provide important clues of medical problems, such as sleep disorders or anomalies, and sudden infant death syndrome (SIDS) of sleeping infants [2]. Most traditional methods for vital sign monitoring require a person to wear special devices such as a capnometer [3] or a pulse oximeter [4]. These technologies are inconvenient to use and uncomfortable. Alternative solutions of contact-free, easy deployment, low-cost, and long-term vital sign monitoring would be highly appealing.

Recently, radio frequency (RF) based vital sign monitoring systems have attracted great interest, which exploits wireless signals to detect breathing-induced chest movement. For example, the Vital-Radio system uses a frequency modulated continuous wave (FMCW) radar to estimate breathing and heart rates [5]. It works for multiple subjects in parallel, but requires a customized hardware with a large bandwidth from 5.46 GHz to 7.25 GHz. Other techniques, such as the Doppler radar [6, 7] and the ultra-wideband radar [8], are also incorporated to monitor vital signs, which also require dedicated hardware with high frequency and high cost. The mmVital system [9] uses the received signal strength (RSS) of 60 GHz millimeter wave (mmWave) signals for breathing and heart rates estimation with a larger bandwidth about 7GHz, which also requires customized hardware and a mechanical rotator. A recent work

1

UbiBreathe monitors the breathing signal using WiFi RSS, which is coarse channel information [10]. UbiBreathe requires a line of sight (LOS) path between the transmitter and receiver, which limits the RF monitoring range in the deployment environment.

Unlike RSS, the channel state information (CSI) represents fine-grained channel information, which is now available for several off-the-shelf WiFi network interface cards (NIC), e.g., Intel WiFi Link 5300 NIC [11] and the Atheros AR9580 chipset [12]. Specifically, CSI consists of both subcarrier-level amplitude and phase information of the orthogonal frequency division multiplexing (OFDM) channel. It is a more stable representation of channel characteristics than RSS. In a recent work [13], the authors use the amplitudes of WiFi CSI data to track vital signs of a sleeping person. However, the CSI phase information has not been used for vital sign monitoring so far, due to large variations caused by noise and the unsynchronized time and frequency at the transmitter and receiver.

1.1 Approach

In this paper, we leverage CSI phase difference data between two antennas of the receiver NIC to detect and monitor breathing rate and heart rate. We find that the CSI phase difference data is quite stable after suitable calibration. Moreover, the CSI phase difference data is also more robust than RSS in various deployment scenarios, such as different distances, obstacles/walls, and orientations. We provide a rigorous analysis of CSI phase difference data, and prove that for indoor multipath environments under small-scale fading, the CSI phase difference data is a periodic signal with the same frequency as the breathing signal, when the wireless signal is reflected from the chest of a person. We also prove that leveraging directional antenna at the transmitter can boost the signal-to-noise ratio (SNR) of CSI phase difference data, thus making it possible to remotely monitor the minute heartbeat signal.

Built upon the analysis, we design PhaseBeat, a remote sensing system using CSI phase difference data for monitoring breathing and heartbeat with commodity WiFi device. First, PhaseBeat exploits the CSI phase difference data to extract the periodic signal induced by chest movements (e.g., inhaling and exhaling). Then, PhaseBeat preprocesses the captured data, with environment detection, data calibration, subcarrier selection, and discrete wavelet

transform. The cleansed CSI phase difference data is then used to estimate the breathing and heart rate in realtime. We implement PhaseBeat with off-the-shelf WiFi devices and evaluate its performance with extensive experiments, which involve four persons over three months in typical indoor environments, such as a computer laboratory, a through-wall scenario, and a long corridor. The experimental results demonstrate that PhaseBeat can achieve high accuracy for breathing and heart rate estimation, with median error of 0.25 bpm and 1 bpm, respectively. We also find PhaseBeat highly robust for breathing rate estimation under various environments, such as different distances between the transmitter and receiver, different distances between the person and the WiFi devices, different orientations and poses, and multiple persons.

The main contributions of this paper are summarized below.

- We theoretically and experimentally validate the feasibility of using CSI phase difference for vital sign monitoring. In particular, we provide a rigorous analysis of the measured CSI phase information, with respect to its stability and periodicity. To the best of our knowledge, this is the first work to exploit CSI phase difference for breathing rate and heart rate estimation.

- We design the PhaseBeat system based on the analysis. We develop several signal processing algorithms for preprocessing the collected CSI phase difference data, which can obtain the denoised breathing signal and the reconstructed heart signal. Then, we employ peak detection and root-MUSIC methods for breathing rate estimation with one person and multiple persons, respectively, and leverage an FFT based method for heart rate estimation.

- We prototype the PhaseBeat system with commodity WiFi devices and validate its superior performance in typical indoor environments with extensive experiments. Our experimental results demonstrate the superior performance of PhaseBeat over traditional CSI amplitude based approach.

3

1.2 Layout

In the remainder of this paper, we present the research background in chapter 2. Preliminaries and our analysis of phase difference data are showed in Chapter 3. We describe the Phase-Beat design in Chapter 4 and demonstrate its performance in Chapter 5. Chapter 6 reviews conclusion and future work about this paper.

Chapter 2

Background

2.1 Introduction of Internet of Things

As we enter the new era of information and electronic, the explosive development of electronic devices and communication technology makes people get access to the internet in mostly anywhere and anytime [14–32]. Now, the next generation of information network is internet of Things(IoT), which means every device, each person, and any piece of data should all be included in a whole internet [33–35]. With IoT technique, everything can upload the information generated or sensed by itself to the internet. Meanwhile, the data can be transmitted to anywhere or stored in database for the further analysis. The specialty of IoT allows people to gather and analyze data of anything inside the network infrastructure much more efficiently than before. Many promising technologies can be fulfilled based on IoT such as healthcare, home remote monitoring and managing, big data analysis for whole country, operation optimization in industry, and big environment monitoring.

2.2 Introduction of IoT Based Healthcare

Among these promising technologies, healthcare attracts more attention from the public, because health is the foundation of peoples daily lives. With the combination of IoT and healthcare the doctor can do remote diagnosis [36]. Traditionally, patients tend to make an appointment and visit our doctor when get sick, which may take us about 2-3 hours or longer before getting diagnosis result. With the help of IoT, people do not need to get out to the hospital. Instead, the doctor can get the information they need from IoT, and patient can also get medical
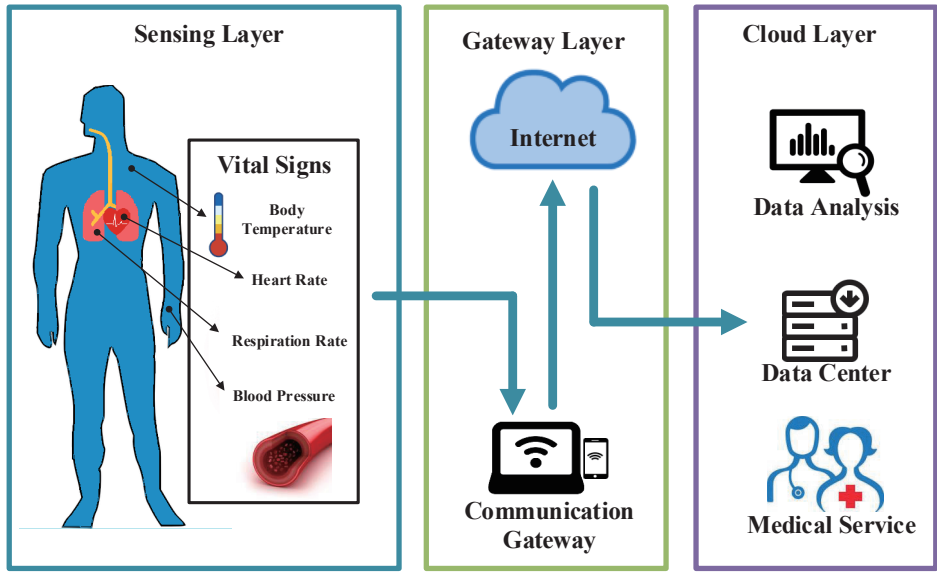
Figure 2.1: IoT based Healthcare System Architecture.

care from the doctor when they stay at home or work in their office. Like ordering products from the website, people can also get medical care without getting out of the door.

In addition to remote diagnosis, IoT based healthcare also includes other applications such as: remote baby monitoring, log-term human body health tacking, and fitness programs planning [36]. These applications are mostly about chronic health problem detection and precaution. It is reported that about 100 million people in the U.S. have chronic problems. Actually, Americans spend a large number of money on their chronic problems, which are almost three fourths of their total health care cost [1]. However, the cost can be highly reduced if there is a suitable precaution. Therefore, a long-term health monitoring system is needed to evaluate the current condition of human, and give the warning to the user if there is a potential risk. With this kind of system, doctors can provide medical suggestions in the time to reduce the cost of the chronic diseases.

2.3 Structure of IoT Based Healthcare

Many remote healthcare works show that, an IoT based healthcare system is usually established by three layers: sensing layer, gateway layer, and cloud layer. [36]The overview of the structure is showed in Fig. 2.1. The first layer is sensing layer, which is mostly responsible for employing different kinds of sensors to extract vital sign signals from human body. The gateway layer will

deal with the extracted signal and then transmit the signal to the Internet for the following layer. The third layer is called cloud layer, which is mainly concerned with data analysis and processing. For example, the doctor can collect all vital signs of their patients and give professional medical suggestions based on the information extracted from the sensing layer, and ask the patient to the hospital for further diagnosis.

To fulfill this type of IoT based healthcare system, there is an increasing demand for various advanced medical sensors to extract the necessary information from users more efficiently than traditional sensors. Instead of traditional measurements, these sensors are considered as smart sensors [36], which are more convenient and accurate. Smart sensors play an important role in IoT based healthcare, because they not only need to monitor human bodies, but also to transmit the extracted signals to the Internet. They are responsible for collecting the source information, which is highly related to the final diagnosis result. Therefore, inventing sensors with high accuracy and convenience has become a popular topic in research field.

2.3.1 Multimedia Sensors in Sensing Layer

The vital signs are extracted in the sensing layer. As we know, four main vital signs are body temperature, heart rate, respiration rate and blood pressure. These four vital signs can reflect health condition of human body, and the traditional measurement of these vital signs have been used by special devices. For instance, people can measure their body temperature by simply using a thermometer. Blood pressure can be measured by a blood pressure cuff and stethoscope. However, even though traditional measurements for vital signals are easy to operate, there are still some challenges when they are employed in the sensing layer. On one hand, most of the traditional measurement devices are wearable, which means patients should keep these measurement tools on their body, like thermometer and stethoscope. These devices are convenient and easy to operate for adults, but they may cause babies and elders feel uncomfortable in some cases. On the other hand, these traditional devices are mostly invented to measure the vital signs within a shot period, so most of them are not suitable for long-term monitoring.

Recently, many multimedia sensors are designed to achieve stable and accurate vital signs measurements. Most of sensors are contact-less and suitable for long-term vital sign monitoring

7

such as RF based sensors [6, 8, 37–40] and other sensing method based on the video taken by a camera [41]. Some sensors are not contact-less but are also comfortable for users to wear it, because these sensors are very small or embedded in smart phone. For example, some techniques use the accelerometer in smart phones to monitor the movement of users [42] and some technologies employ RFID tag to extract breathing signals [37]. This paper will introduce some typical technologies for these multimedia sensors.

Radar Monitoring

For radar techniques, there are several types of radar systems such as: Doppler radar [6], ultrawideband(UWB) radar, and FMCW radar system. In Doppler radar system, the authors leverage a CMOS Doppler radar to extract respiratory signal and heart beat signal. The experiments show that the effective distances for measuring heart rate and respiration rate are 1 m and 1.5 m, respectively. The measurement accuracy is related to the SNR of Doppler Radar. With suitable measuring distance and best SNR the measuring error for both heart rate and breathing rate is about 1 bpm.

For UWB radar, the system is designed to measure the propagation of UWB radio signal between two antenna arrays [8]. The authors use arrays to transmit and receive RF signal instead of single antenna for better accuracy. With MIMO technique, the radar system can achieve higher accuracy when tracking the movement and position of human. Moreover, the radar works in 2-8 GHz frequency range. The breathing rate is estimate by reproducing UWB channel generated by environment changes, which is caused by the movement of human breath. The measurement is fulfilled by using Vector Network Analyzer(VNA) and virtual antenna arrays technique. The system is tested both in LOS and NLOS case, and the results show that the system can track the movement of the human chest within the range about 5 m.

Recently FMCW radar is also used in monitoring vital signals [38]. The authors develop a Vital-Radio system to monitor the breathing and heart rates of human. The system is operated by transmitting wireless signals and recording the time before the reflection comes back.

The system can monitor multiple people simultaneously because of the frequency modulated carrier wave (FMCW) technique. As Fig. 2.2 shows, different reflectors will cause

8
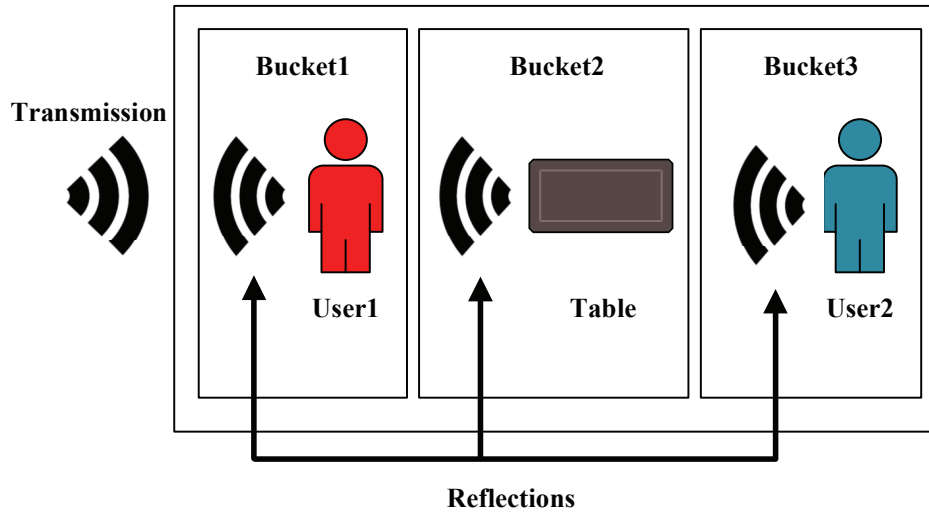
Figure 2.2: Reflectors in Different Distance for FMCW Radar.

different reflection time, because the distance from the reflectors to the transmitter is different. FMCW radar can modulate the frequency before transmitting the wireless signal, so that the system can separate users with different distance in corresponding buckets. In the measurement part, both breathing rate and heart rate are estimated by FFT, but the final result is calculated by using the slope of invers FFT for higher resolution compared with normal FFT. The median accuracy of the system is high up to 99 percent, and the effective distance is 8 meters. The experiments show that the system can also operate when the radar and users are in different rooms.

These radar techniques are all good at monitoring breathing signals with contactless radar device. With FMCW technique, the radar can also measure human heart rates, and monitor vital signs for multiple people. However, these radar techniques require special hard device to transmit and receiver signal.

Channel State Information Implementation

Some techniques can use WiFi signals to extract the vital signals for users such as respiration rate and heart rate based on channel state information extracted by modified device driver [43–45]. The technique is established by two computers equipped with Intel 5300 NIC, where one is set as a receiver and another one is set as a transmitter. Different from other technique, WiFi monitoring system does not require any special hardware. The papers show that both amplitude

and phase difference of CSI can be implemented to monitor human breathing movement. In this paper, we will introduce the sleeping breath monitoring system, which uses the amplitude of CSI to detect the respiration signal.

The system implements a WiFi device to receive packets sent by the access point, and extract channel state information. Then the system will identify the event of the user, such as go to bed, get up and turnover. The breathing rate and heart rate can be estimated after the data from human event is filtered out, because large noise caused by the sleep event will highly decrease the SNR. After the signal is calibrated, the respiration rate for single person is estimated by peak detection algorithm, meanwhile, the breathing rates for two persons can also be estimated by K-means clustering based on Power Spectral Density(PSD). The signal related to heart beats is extracted by using band pass filter, where the heart rate is estimated by applying peak determination in PSD measurement.

Monitoring with Camera

The photoplethysmography(PPG) has already been a main technique and widely used in daily lives. As we know, PPG can monitor the heart rate by measuring the light absorption signal, which is caused by blood volume changes. However, traditional PPG is not suitable for long range monitoring because the system needs to extract the light signal from the blood vessel with directly attached camera. To extract the PPG from the user remotely, some techniques can monitor vital sign including breathing rate and heart rate and SpO2 by analyzing the video taken by an off-the-shelf camera.

One typical system is established as the Fig. 2.3 shows above [41]. The movement of the user is recorded by a camera, where the image is generated by the ambient light. The resolution is 8 bits per pixel and the sampling rate is 12 Hz. The first step is using features tracking technique to separate the frame in several segments such as users head. After that, some regions of interest(ROI) are extracted from different segments. These ROI are divided in two types: one is subject ROI (ROIs), like forehead and cheek of the user face, which can represent subjects information. Another one is called reference ROI (ROIr), which can represent the
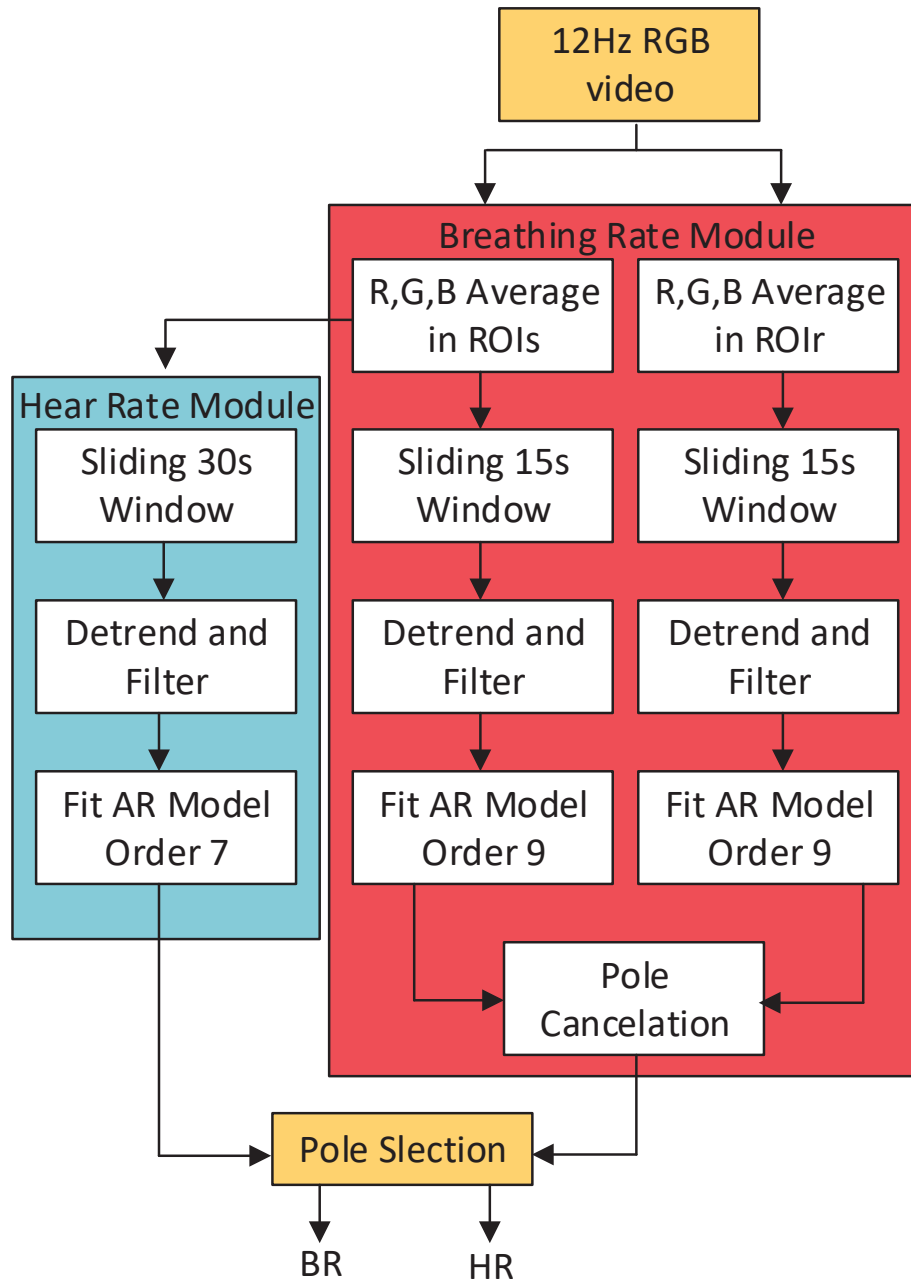
Figure 2.3: Camera Based Health Sensing System Structure.

background signal. After ROI extraction, the RGB channel information within a sliding window are extracted for the following processing, like detrending and filtering. Different from other measuring methods, the frequency of the target vital signal is estimated by AR modeling instead of Fourier transform. Before getting the final vital signal the authors also propose a pole cancellation method to suppress the unrelated components in AR modeling result, which is caused by low sampling frequency.

There is also another technique, which focuses on monitoring the heart rate by using the camera embedded in the off-the-shelf smart phone [46]. Camera of the mobile phone can record and analyze the color signals when the user puts their finger on the flash light and covers the camera at the same time. Even though the sensor is not contactless, the sensor is also very convenient for human because of the high portability of mobile phone.

Different from RF signal monitoring system, vital signals monitoring is hardly affected by others users movement because camera can easily focus on one user. However, most of the camera techniques rely on stable illumination. When the light source is not stable, or the monitoring environment is too dark, the accuracy of measurement results will decline greatly.

Sensing based on Accelerometer

Another technique called Zephyr can measure the human breathing rate by using the redundant data generated from the accelerometer and gyroscope embedded in smartphones [42]. As smartphones are widely used in human daily life, Zephyr is convenient for monitoring the respiration rate for a long term although the accelerometer sensor is not contact-less.

The raw data is collected from different axis for both accelerometer and gyroscope (six sensors totally) to improve the accuracy of breathing beats estimation. To obtain the smooth signal for respiration rate estimation the authors implement a Hilbert Transform based method to estimate the envelope of the signal, which applies a local mean removal technique to reduce the sudden change influence. The breathing rates from all six sensors are estimated independently by FFT and eventually fused into single result by employing Kalman Filter-based fusion technique. The last step of the system is to get a robust breathing rate result instead of unstable instantaneous data by using alpha-trimmed filter.

The authors also test the system in various users. The experimental results show that the median error of the final respiration results is 0.04 bpm and the maximum error is less than 2 bpm, which proves that the system is robust for different users.

2.3.2 Gateway Layer Introduction

Gateway layer can collect the data coming from all kinds of smart sensors and then transmit the data to the cloud through wide area network(WAN) [47]. In gateway layer, the data can be sent to the cloud with either physical interface or wireless interface. For the convenience and flexibility of the whole IOT network the wireless transmission is more suitable for different kinds of IOT structures than wired transmission. The gateway is also responsible for the safety and stability during data transmission. Considering multiple sensors and lots of users within IoT healthcare system, the gateway should be also able to read health data from different sensors and deal with the collision happened when large number of data are sent at a small period of time.

2.3.3 Cloud Layer Introduction

In cloud layer, the collected health data can be stored in database, and can be analyzed by professional organizations [36, 47]. The function of a healthcare system is to provide healthcare solution based on various users health conditions. As a IoT based healthcare system, the medical service mostly focuses on two parts. The first part is health condition monitoring for individuals, which is concerned with monitoring different kinds of diseases threaten. To make the long-term monitoring becomes convenient for the users, the smart health evaluation system should be developed to evaluate the health condition based on users body information for several months or several years. The second part is about precaution for a special disease in a large group of people, which can highly reduce the influence in the future for society. This function is related to the big data analysis technique, where many algorithms and data structures are proposed to achieve high accuracy and high efficiency in potential disease prediction.

Chapter 3

Preliminaries and Phase Difference Analysis

3.1 Channel State Information Preliminaries

OFDM is widely used in modern wireless network standards, such as WiFi (i.e., IEEE 802.11 a/g/n) and LTE [27,48,49]. With OFDM, the total spectrum is partitioned into multiple orthogonal subcarriers, and wireless data is transmitted over the subcarriers using the same modulation and coding scheme (MCS) to mitigate frequency selective fading. Leveraging the device driver for off-the-shelf NICs, e.g., the Intel 5300 NIC [11], we can extract the CSI from the NIC, which is fine-grained physical layer (PHY) information. CSI reveals the channel characteristics experienced by the received signal such as the multipath effect, shadow fading, and distortion [48].

With OFDM, the WiFi channel at the 5 GHz band can be considered as a narrowband flat fading channel. In the frequency domain, the channel model can be expressed as $\vec{Y} = \text{CSI} \cdot \vec{X} + \vec{N}$, where $\vec{Y}$ and $\vec{X}$ denote the received and transmitted signal vectors, respectively, $\vec{N}$ is the additive white Gaussian noise, and CSI represents the channel's frequency response, which can be estimated from $\vec{Y}$ and $\vec{X}$.

Although the WiFi OFDM system has 56 subcarriers over a 20 MHz channel, the Intel 5300 NIC can report CSI for only 30 of the 56 subcarriers. The channel frequency response of subcarrier i, CSI_i, is a complex value, that is

$$\text{CSI}_i = \mathcal{I}_i + j\mathcal{Q}_i = |\text{CSI}_i| \exp\left(j\angle\text{CSI}_i\right), \tag{3.1}$$

where $\mathcal{I}_i$ and $\mathcal{Q}_i$ are the in-phase component and quadrature component, respectively; $|\text{CSI}_i|$ and $\angle\text{CSI}_i$ are the amplitude response and phase response of subcarrier i, respectively.

For an indoor environment with NLOS components [44], the channel frequency response of subcarrier i can also be formulated as

$$\text{CSI}_i = \sum_{k=0}^{K} r_k \cdot e^{-j2\pi f_i \tau_k}. \tag{3.2}$$

where K is the number of multipaths, r_k and τ_k are the attenuation and the propagation delay from the k_{th} path, respectively, and f_i is the central frequency of subcarrier i. Traditionally, the multipaths are harmful for indoor localization, because only the LOS component is a good indicator of distance [44,50]. However, our PhaseBeat system can effectively exploit the reflections for vital signals monitoring, as will be shown in this paper.

3.2 Phase Difference Information

In this section, we show that the CSI phase difference data between two antennas for consecutive packets of the 5 GHz OFDM channel is highly stable and a periodic signal with the same frequency as the breathing signal. We now provide an analysis to validate the stability from the measured phase difference. Let $\angle\widehat{CSI}_i$ denote the measured phase of subcarrier i, which is given by [12,51–54]

$$\angle\widehat{CSI}_i = \angle\text{CSI}_i + (\lambda_p + \lambda_s)m_i + \lambda_c + \beta + Z, \tag{3.3}$$

where $\angle\text{CSI}_i$ is the true phase value, m_i is the subcarrier index of subcarrier i, β is the initial phase offset due to the phase-locked loop (PLL), Z is the measurement noise that is assumed to be AWGN of variance σ^2, and λ_p, λ_s and λ_c are the phase errors from the packet boundary detection (PBD), the sampling frequency offset (SFO), and central frequency offset (CFO), respectively [51]. The phase errors can be written as

$$\lambda_p = 2\pi\frac{\Delta t}{N}, \lambda_s = 2\pi\left(\frac{T'-T}{T}\right)\frac{T_s}{T_u}n, \lambda_c = 2\pi\Delta f T_s n, \tag{3.4}$$

15

where Δt is the packet boundary detection delay, N is the FFT size, T' and T are the sampling periods at the receiver and the transmitter, respectively, T_u is the length of the data symbol, T_s is the total length of a data symbol and the guard interval, n is the sampling time offset for the current packet, and Δf is the center frequency difference between the transmitter and receiver. Note that we cannot obtain the exact values for Δt, $\frac{T'-T}{T}$, n, Δf, and β in (3.3) and (3.4). Moreover, λ_p, λ_s, and λ_c vary for different packets with different Δt and n. Thus, the true phase $\angle\mathrm{CSI}_i$ cannot be derived from the measured phase value. Fortunately, the measured *phase difference* on subcarrier i can be leveraged as in the following theorem.

Theorem 1. *The measured phase difference on subcarrier i between two receiver antennas is stable, and its mean and variation are given by*

$$\begin{cases} \mathbb{E}(\Delta\angle\widehat{CSI}_i) = \mathbb{E}(\Delta\angle CSI_i) + \Delta\beta \\ Var(\Delta\angle\widehat{CSI}_i) = Var(\Delta\angle CSI_i) + 2\sigma^2. \end{cases} \tag{3.5}$$

Proof. Note that the three antennas of the Intel 5300 NIC use the same clock and the same down-converter frequency. Consequently, the measured phases of subcarrier i from two antennas have identical packet detection delay, sampling periods, frequency differences, and the same index m_i [55]. Thus the measured phase difference on subcarrier i between two antennas can be approximated as

$$\Delta\angle\widehat{CSI}_i = \Delta\angle\mathrm{CSI}_i + \Delta\beta + \Delta Z, \tag{3.6}$$

where $\Delta\angle\mathrm{CSI}_i$ is the true phase difference of subcarrier i, $\Delta\beta$ is the unknown difference in phase offsets, which is in fact a constant [55], and ΔZ is the noise difference with variance $2\sigma^2$. Since Δt, Δf, and n are all removed, $\Delta\angle\widehat{CSI}_i$ in (3.6) becomes highly stable for consecutive packets. From (3.6), we can derive the mean and variance of the measured phase difference on subcarrier i as that given in (3.5). $\qquad\square$

From (3.6), it can be seen that $\mathbb{E}(\Delta\angle\widehat{CSI}_i) - \mathbb{E}(\Delta\angle\mathrm{CSI}_i)$ is a constant $\Delta\beta$. The difference does not change the estimated frequency of vital signals, although its variance becomes
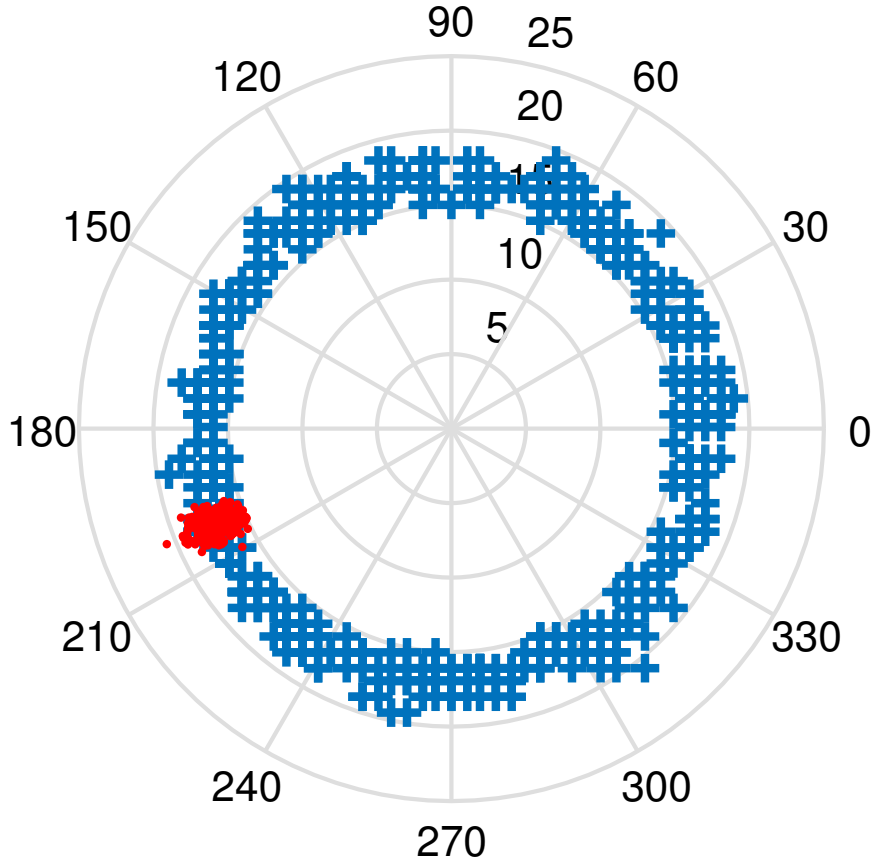
Figure 3.1: Comparison between phase CSI measured from a single antenna (marked as blue crosses) and the phase differences measured from two antennas (marked as red dots) of the 5th subcarrier for 600 consecutively received packets.

larger. Fig. 3.1 is a comparison between the single antenna phases (as blue crosses) and the phase differences (as red dots) of the 5th subcarrier in the polar coordinate plot for 600 consecutively received packets. We can see that the single antenna phase of the 5th subcarrier is nearly uniformly distributed between $0°$ and $360°$, making it unusable. However, all phase difference data of the 5th subcarrier concentrate into a sector between $190°$ and $210°$, which clearly validates Theorem 1.

In the following Theorem, we show the measured phase difference information is periodic.

Lemma 1. *When the wireless signal is reflected from the chest of a person with a breathing frequency f_b, the true phase of the reflected signal at any antenna of the receiver is also periodic with the same frequency f_b.*

Proof. Because the wireless signal on subcarrier i is a plane wave, its true phase at the receiver is determined by the propagation distance, that is $\angle\text{CSI}_i = 2\pi d(t)/\lambda_i$, where $d(t)$ is the propagation distance at time t and λ_i is the wavelength of subcarrier i. When the chest of a person periodically rises and falls with frequency f_b, the propagation distance $d(t)$ of the reflection signal becomes $d(t) = D + A\cos(2\pi f_b t)$, where D is the constant mean distance of the reflection path, A is the amplitude of the periodic signal from chest movements. Thus, the true phase of the reflected signal at the receiver is $\angle\text{CSI}_i = 2\pi(D + A\cos(2\pi f_b t))/\lambda_i$. Clearly, the true phase at the receiver is a periodic signal with the frequency f_b. $\qquad\square$

Theorem 2. *For indoor environments with multipaths, when the wireless signal is reflected from the chest of a person with breathing frequency f_b, the true phase at any antenna of the receiver is also a periodic signal with frequency f_d such that*

$$P\left(|f_d - f_b| < \epsilon\right) = 1, \quad \forall \epsilon > 0. \tag{3.7}$$

Proof. Based on Lemma 1, the true phase of the reflected signal at the receiver, $\angle\text{CSI}_i = 2\pi(D + A\cos(2\pi f_b t))/\lambda_i$ is periodic with frequency f_b. Let the reflected signal be the dynamic component, and the sum of other LOS and multipath signals as the static component. We can rewrite (3.2) as

$$
\begin{aligned}
\text{CSI}_i &= \sum_{k=0, k\neq d}^{K} r_k \cdot e^{-j2\pi f_i \tau_k} + r_d \cdot e^{-j2\pi f_i \tau_d} \\
&= |\text{CSI}_i^s| \exp\left(j\angle\text{CSI}_i^s\right) + |\text{CSI}_i^d| \exp\left(j\angle\text{CSI}_i^d\right),
\end{aligned}
\tag{3.8}
$$

where CSI_i^s is the static component given as $\sum_{k=0, k\neq d}^{K} r_k \cdot e^{-j2\pi f_i \tau_k}$, CSI_i^d is the dynamic component given as $r_d \cdot e^{-j2\pi f_i \tau_d}$. Moreover, $\angle\text{CSI}_i^d$ is a periodic signal with frequency f_b, and $|\text{CSI}_i^s|$, $\angle\text{CSI}_i^s$ and $|\text{CSI}_i^d|$ are considered to be constants.

To obtain the phase of CSI_i, we illustrate the geometric relationship among the static component CSI_i^s, the dynamic component CSI_i^d, and the total component CSI_i using an *in-phase-quadrature* (I-Q) plot in Fig. 3.2. From Fig. 3.2, we can easily obtain the angle $\angle\text{DST} = \angle\text{CSI}_i^s - \angle\text{CSI}_i^d$, the length $OT = |\text{CSI}_i^d|\cos(\angle\text{CSI}_i^s - \angle\text{CSI}_i^d) + |\text{CSI}_i^s|$, and the length $TD =$

$|\text{CSI}_i^d|\sin(\angle\text{CSI}_i^s - \angle\text{CSI}_i^d)$. Thus, the phase of the total component CSI_i can be computed as

$$\angle\text{CSI}_i = \angle\text{CSI}_i^s - \arctan\frac{|\text{CSI}_i^d|\sin(\angle\text{CSI}_i^s - \angle\text{CSI}_i^d)}{|\text{CSI}_i^d|\cos(\angle\text{CSI}_i^s - \angle\text{CSI}_i^d) + |\text{CSI}_i^s|}. \tag{3.9}$$

Because $\angle\text{CSI}_i^d$ is periodic, $\angle\text{CSI}_i$ is also periodic. To show that the frequency of the total phase $\angle\text{CSI}_i$ is f_b, we differentiate (3.9) and set the derivative to zero. We then have

$$\cos(\angle\text{CSI}_i^s - \angle\text{CSI}_i^d) = -|\text{CSI}_i^d|/|\text{CSI}_i^s|. \tag{3.10}$$

The solution is $\angle\text{CSI}_i^d = \angle\text{CSI}_i^s + \pi - \arccos(|\text{CSI}_i^d|/|\text{CSI}_i^s|)$ (vector $S\vec{D}_2$) or $\angle\text{CSI}_i^d = \angle\text{CSI}_i^s + \pi + \arccos(|\text{CSI}_i^d|/|\text{CSI}_i^s|)$ (vector $S\vec{D}_1$), as shown in Fig. 3.2. When the phase $\angle\text{CSI}_i^d \in \{\angle\text{CSI}_i^s + \pi + \arccos(|\text{CSI}_i^d|/|\text{CSI}_i^s|) - 2\pi, \angle\text{CSI}_i^s + \pi - \arccos(|\text{CSI}_i^d|/|\text{CSI}_i^s|)\}$, (3.9) is an increasing function; otherwise, it is a decreasing function. Thus, except for the only two points D_1 and D_2, the phase of the total component CSI_i is periodic with frequency f_b. Moreover, since the true phase CSI_i is continuous, the probability that the true phase CSI_i stays exactly at points D_1 or D_2 equals to zero. Thus Theorem 2 holds true. $\qquad\square$

Now consider another antenna. With the same analysis, we can also obtain (3.9) for the additional antenna, which is also periodic with frequency f_b. However, its the static component CSI_i^s and the dynamic component CSI_i^d on subcarrier i that are different, due to the different positions of the two antennas. This is true for any pair of antennas of the three-antenna Intel 5300 NIC. We thus conclude that the true phase difference between any pair of antennas is a periodic signal with the frequency f_b.

Following Theorem 1 and (3.6), we can easily show that the measured phase difference on subcarrier i between two antennas is also a stable periodic signal with frequency f_b, although the waveform of the signal is attenuated due to increased noise. To improve the signal waveform, directional antennas can be used at the transmitter, which can strengthen the power of the reflected signal from the human body. In our PhaseBeat system, we adopt a directional antenna at the transmitter for heart rate monitoring, because the heartbeat introduced effect on

Figure 3.2: Illustration of the geometric relationship among the static component CSI_i^s (the green vector $\vec{OS}$), the dynamic component CSI_i^d (the red vector $\vec{SD}$), and the total component CSI_i (the blue vector $\vec{OD}$) in the I-Q plot.

the reflected signal is extremely weak. To reveal the effect of directional antennas, we derive the following corollaries based on Theorem 2 and (3.9).

Corollary 2.1. *When the ratio $|CSI_i^d|/|CSI_i^s| \rightarrow \infty$, the true phase of subcarrier i at a receiver antenna becomes a periodic signal with frequency f_b, and the true phase of subcarrier i becomes $\angle CSI_i = \angle CSI_i^d$.*

Proof. According to (3.9), we can easily obtain $\angle CSI_i = \angle CSI_i^d$ when the ratio $|CSI_i^d|/|CSI_i^s| \rightarrow \infty$. Moreover, $\angle CSI_i^d$ is a periodic signal with frequency f_b, and thus the corollary is proven.

$\square$

Corollary 2.2. *When the ratio $|CSI_i^d|/|CSI_i^s| \to 0$, the true phase of subcarrier i at a receiver antenna will not be periodic, and the true phase of subcarrier i becomes $\angle CSI_i = \angle CSI_i^s$.*

Proof. According to (3.9), we can easily obtain $\angle \mathrm{CSI}_i = \angle \mathrm{CSI}_i^s$ when the ratio $|\mathrm{CSI}_i^d|/|\mathrm{CSI}_i^s| \to$ 0. Moreover, $\angle \mathrm{CSI}_i^s$ is not a periodic signal. Thus the corollary is proven. $\qquad\square$

Following Corollaries 2.1 and 2.2, it can be seen that when the reflection from the chest becomes strong, the waveform of the received signal is periodic with a high SNR; when the chest reflection becomes weak, the waveform of the received signal is still periodic but with a low SNR. Thus, it is still challenging to estimate the breathing rate and heart rate based on the reflected signal, due to multipaths, obstacles, long distance between the person and the receiver, and low SNR. In the following section, we describe the design of the PhaseBeat system, aiming to overcome the above challenges for estimating breathing rate and heart rate using CSI phase difference data, for one or more persons.

Chapter 4

The PhaseBeat System

4.1   PhaseBeat System Architecture

We design the PhaseBeat system to monitor vital signs such as breathing and heartbeat of one or more persons by leveraging CSI phase difference data with commodity WiFi devices. Specifically, PhaseBeat exploits CSI phase difference data to extract the periodic signal caused by the rise and fall of the chest (e.g., inhaling and exhaling). Based on Theorems 1 and 2, PhaseBeat can effectively exploit CSI phase difference data to monitor vital signs. First, CSI phase difference data is relatively stable for back-to-back packets in stationary environments such as people sitting, standing, or sleeping. It can thus be effective for monitoring vital signs. Second, CSI phase difference data includes the periodic signal that has the same frequency as the breathing signal. Finally, the CSI phase difference data is more robust, with only small variations for different distances or different orientations, compared with CSI amplitude data used in prior work for monitoring vital signs.

The PhaseBeat system architecture is presented in Fig. 4.1. It includes four basic modules: Data Extraction, Data Preprocessing, Breathing Rate Estimation, and Heart Rate Estimation. The Data Extraction module extracts CSI phase difference data between two receive antennas of an off-the-shelf WiFi device. The Data Preprocessing module consists of environment detection, data calibration, subcarrier selection, and discrete wavelet transform. For environment detection, we adopt a threshold method to determine the stationary states of a person, such as sitting, standing, or sleeping. For data calibration, we remove the direct current (DC) component and high frequency noises, and downsample the processed data. Then, subcarrier selection
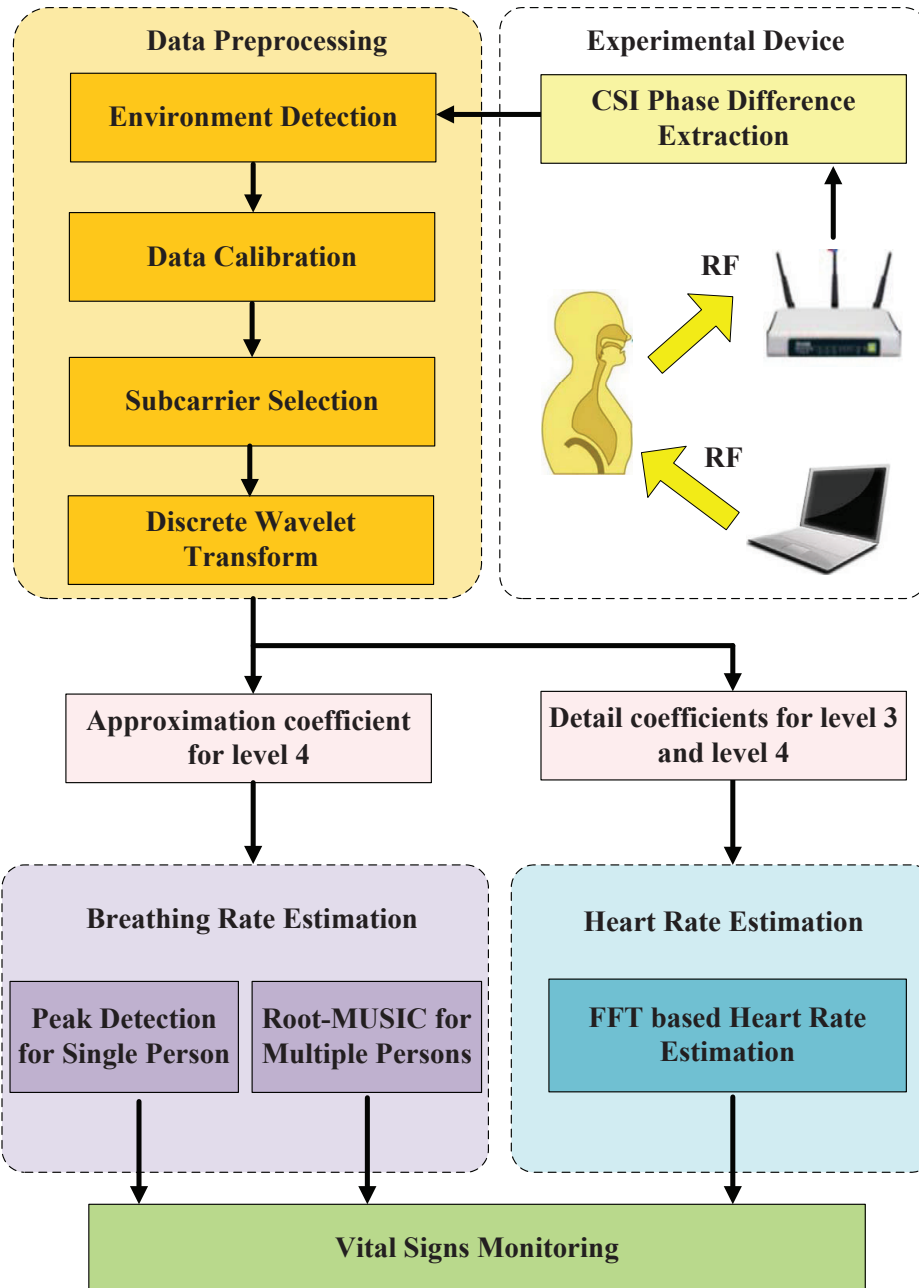
Figure 4.1: PhaseBeat system architecture.

is used to improve the reliability of CSI phase difference data. The discrete wavelet transform (DWT) is used to obtain the denoised breathing signal with approximation coefficient for level 4 and the reconstructed heart signal with the sum of detail coefficients for level 3 and level 4. In the Breathing Rate Estimation module, we use peak detection for the case of a single person and the root-MUSIC method for the case of multiple persons. In the Heart Rate Estimation module, we use an FFT based method to detect the heart rate.

4.2 Data Preprocessing

4.2.1 Environment Detection

After extracting the CSI phase difference information using (3.6), we need to determine whether the person is in a stationary state. When the person is determined to be in a stationary state, such as sitting, standing, or sleeping, PhaseBeat can estimate his/her breathing rate and heart rate. A threshold-based method is used to identify whether a segment of CSI phase difference data is received in a stationary state, by computing the mean absolute deviation of the CSI phase difference data in a short sliding window.

We define V as the sum of mean absolute deviations of all CSI phase difference data in the sliding window as

$$V = \frac{1}{|W|} \sum_{i=1}^{30} \sum_{k \in W} |\Delta \angle \widehat{CSI}_i(k) - \mathbb{E}(\Delta \angle \widehat{CSI}_i(k))|, \tag{4.1}$$

where $\Delta \angle \widehat{CSI}_i(k)$ is the measured phase difference from subcarrier i for packet k, W is the index set of all the packets in the sliding window, $|W|$ is the length of the sliding window. Because other movement events lead to larger variations in CSI phase difference data than that caused by the minute movements of breathing and heartbeat, the threshold-based approach is effective to detect such large movements (such as walking or jumping). In PhaseBeat, we set the threshold between 0.25 and 6 to identify useful data for vital sign monitoring. Fig. 4.2 shows the environment detection results for different states. When the person is sitting, the phase difference data is a sinusoidal-like periodic signal over time. When there is no one in the range, the phase difference data is a straight line with very small fluctuations. When the person stands up or is walking, the phase difference data exhibits larger fluctuations. Thus, a simple threshold can be effective to determine the stationary state of the person.

4.2.2 Data Calibration

To obtain robust CSI phase difference data, we further perform data calibration to remove the DC component and high frequency noises, and to downsample the processed data. First,
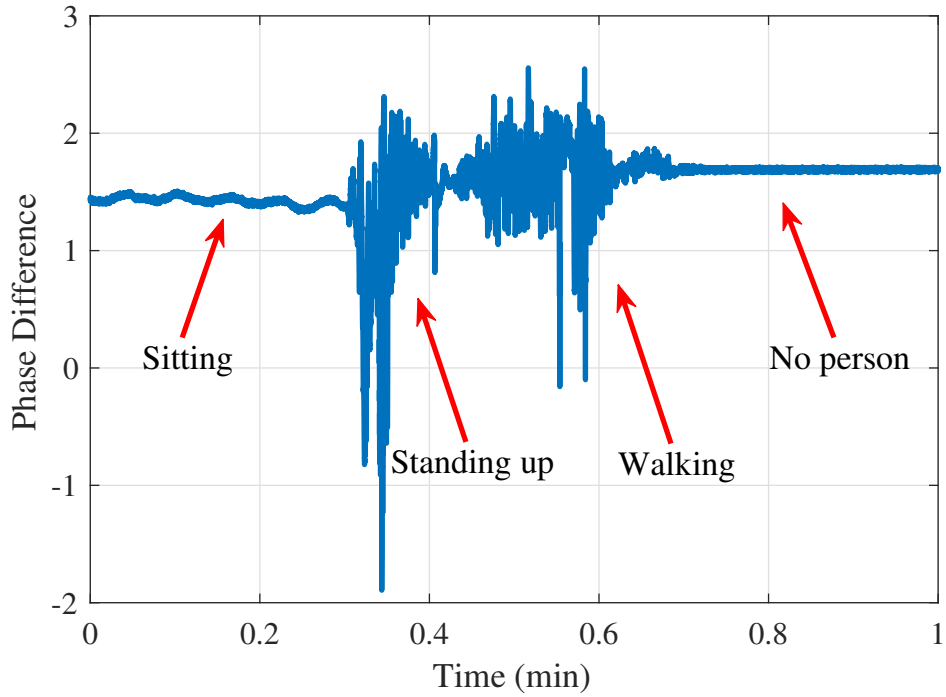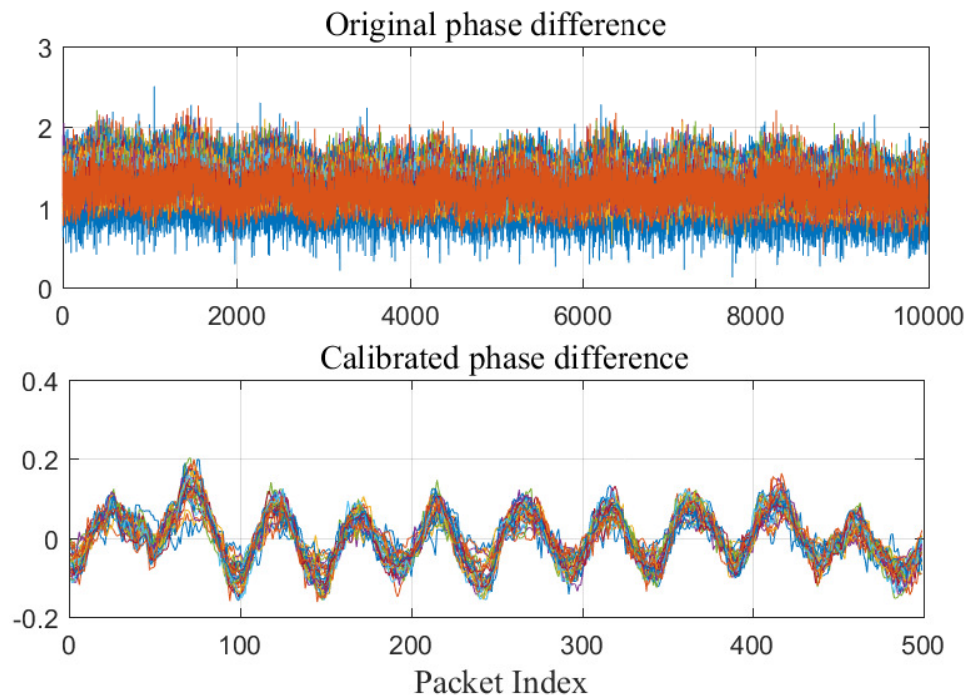
Figure 4.2: Environment detection.

Figure 4.3: Data calibration.

because the DC component affects subcarrier selection, peak detection, and FFT frequency estimation, PhaseBeat needs to remove the DC component with the Hampel Filter. Unlike traditional data calibration methods that only remove high frequency noises, we use the Hampel Filter for detrending of the original CSI phase difference data to remove the DC component.
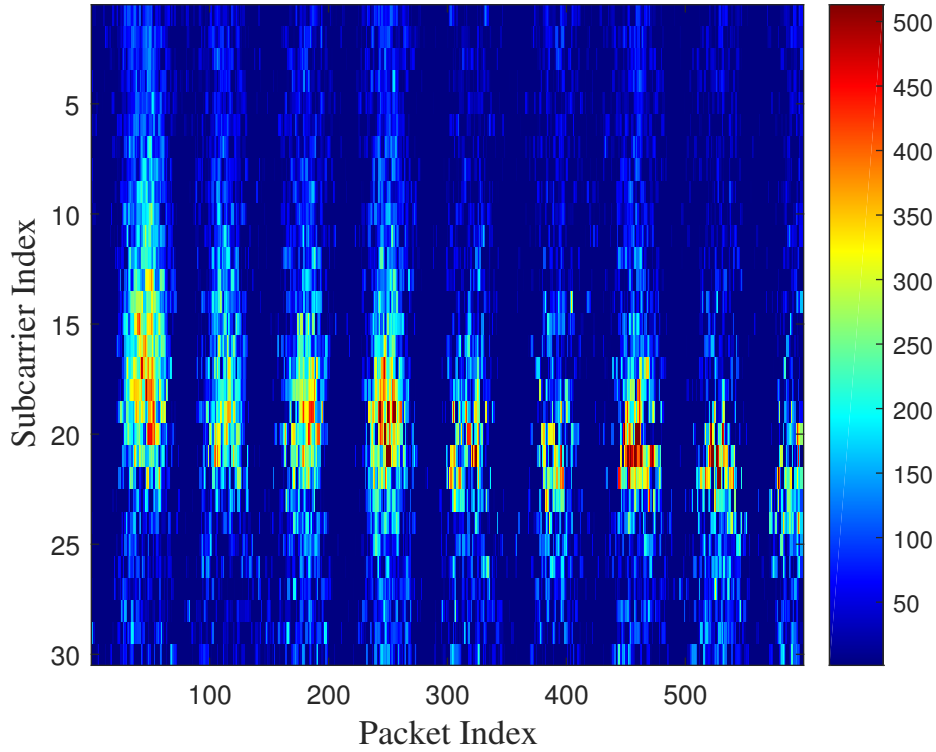
Figure 4.4: CSI phase difference series patterns after data calibration.

The Hampel Filter is utilized to obtain the basic trend of the original data, which is set as a large sliding window with 2000 samples and a small threshold of 0.01. Then, the detrended data is obtained by subtracting the basic trend data from the original data. In addition, we also leverage the Hampel Filter to reduce high frequency noises using a smaller sliding window with 50 samples and the same threshold of 0.01. Second, because PhaseBeat employs a data sample rate of 400 Hz, we need to implement downsampling to reduce the computation complexity for realtime breathing and heart rate estimation. We use a sampling interval of 20 to obtain the low frequency CSI phase difference data, that is equivalent to sampling at 20 Hz.

Fig. 4.3 presents the data calibration results. It can be seen that the original phase differences of all subcarriers have a DC component and high frequency noises. By implementing the proposed data calibration scheme, both the DC component and high frequency noises are removed; the CSI from each of the subcarriers becomes a sinusoidal-like periodic signal over the packets with low noise; and the number of packets is decreased from 10000 to 500, which is amenable to applying other signal processing methods.

26

4.2.3 Subcarrier Selection

PhaseBeat employs subcarrier selection to further boost the reliability of CSI phase difference data, because different subcarriers have different wavelengths, leading to the different sensitivity for breathing and heart signals. We use the mean absolute deviation of CSI phase difference data from every subcarrier to measure its sensitivity. Generally the larger the mean absolute deviation, the higher the sensitivity. Thus, we first choose k maximum mean absolute deviations of CSI phase difference data. Then, we use the median of the k mean absolute deviations of CSI phase difference data to make the final selection. Fig. 4.4 shows the CSI phase difference series patterns after data calibration. We can see that the neighboring subcarriers of subcarrier 20 have higher sensitivity to breathing signals. Then, as shown in Fig. 4.6, the mean absolute deviation of CSI phase difference data of subcarrier 19 is the maximum. In PhaseBeat, we set the $k = 3$ as the default value, and subcarriers 19, 18, and 2 are thus selected. With the above approach, subcarrier 18 is finally selected, which has the highest sensitivity as shown in Fig. 4.6.

4.2.4 Discrete Wavelet Transform (DWT)

Different from FFT and short time Fourier transform (STFT), DWT can achieve a data time-frequency representation, which provides not only the optimal resolution both in the time and frequency domains, but also a multi-scale analysis of the data. With DWT, the phase difference data after subcarrier selection can be decomposed into an *approximation coefficients* vector with a low-pass filter and a *detail coefficients* vector with a high-pass filter. In fact, the approximation coefficient vector represents the basic shape of the input signal with large scale characteristics, while the detail coefficient vector describes the high frequency noises and the detailed information with small scale characteristics.

In wavelet decomposition, the following steps recursively split the previous approximation coefficient and detail coefficient into two new coefficients based on the same scheme [56]. After L steps, the DWT can obtain an approximation coefficient α^L and a sequence of detail

coefficients $\beta^1, \beta^2, ..., \beta^L$. We can compute the DWT coefficients as follows.

$$
\begin{cases}
\alpha_k^{(L)} = \sum_{n\in\mathbb{Z}} \Delta\angle\widetilde{CSI}(n)\phi_{n-2^L k}^{(L)}, \ L \in \mathbb{Z} \\
\beta_k^{(l)} = \sum_{n\in\mathbb{Z}} \Delta\angle\widetilde{CSI}(n)\psi_{n-2^l k}^l, \ l \in \{1,...,L\}\,,
\end{cases}
\tag{4.2}
$$

where $\Delta\angle\widetilde{CSI}(n)$ is the phase difference data after subcarrier selection, $\mathbb{Z}$ is the integer set, the ϕ's and ψ's are wavelet basis functions, which are orthogonal to each other. The phase difference data $\Delta\angle\widetilde{CSI}(n)$ can be approximated using inverse DWT, as

$$
\Delta\angle\widetilde{CSI}(n) = \sum_{k\in\mathbb{Z}} \alpha_k^{(L)}\phi_{n-2^L k}^{(L)} + \sum_{l=1}^{L}\sum_{k\in\mathbb{Z}}\beta_k^{(l)}\psi_{n-2^l k}^l.
\tag{4.3}
$$

In PhaseBeat, DWT is employed to remove high frequency noises from the collected CSI phase difference data. Moreover, the approximation coefficient α^L is used to detect the breathing rate, while the sum of detail coefficients $\beta^{L-1} + \beta^L$ is used to detect the heart rate. We set L to 4 in this paper. As shown in Fig. 4.5, for the original signal, we first implement the DWT based decomposition recursively for four levels with the Daubechies(db) wavelet filter. Because we obtain a 20 Hz sampling rate after data calibration, and the sampling rate is halved after every step of decomposition, the detail coefficient β^1 and the approximation coefficient α^1 have a frequency ranging from 10 Hz to 5 Hz and 0 Hz to 5 Hz, respectively. Then, the approximation coefficient α^4 has a frequency in 0 Hz to 0.625 Hz to obtain the denoised breathing signal. The sum of detail coefficients $\beta^3 + \beta^4$ has the range from 0.625 Hz to 2.5 Hz to reconstruct the heart signal.

4.3 Breathing Rate Estimation

4.3.1 Peak Detection for the One Person Case

The breathing signal is caused by the small, periodic movement of inhaling and exhaling, which can be extracted from the phase difference data according to Theorem 2. Although the FFT based method can be used to estimate the breathing rate, the accuracy may not be good. This is because the frequency resolution depends on the window size of FFT. If the window size
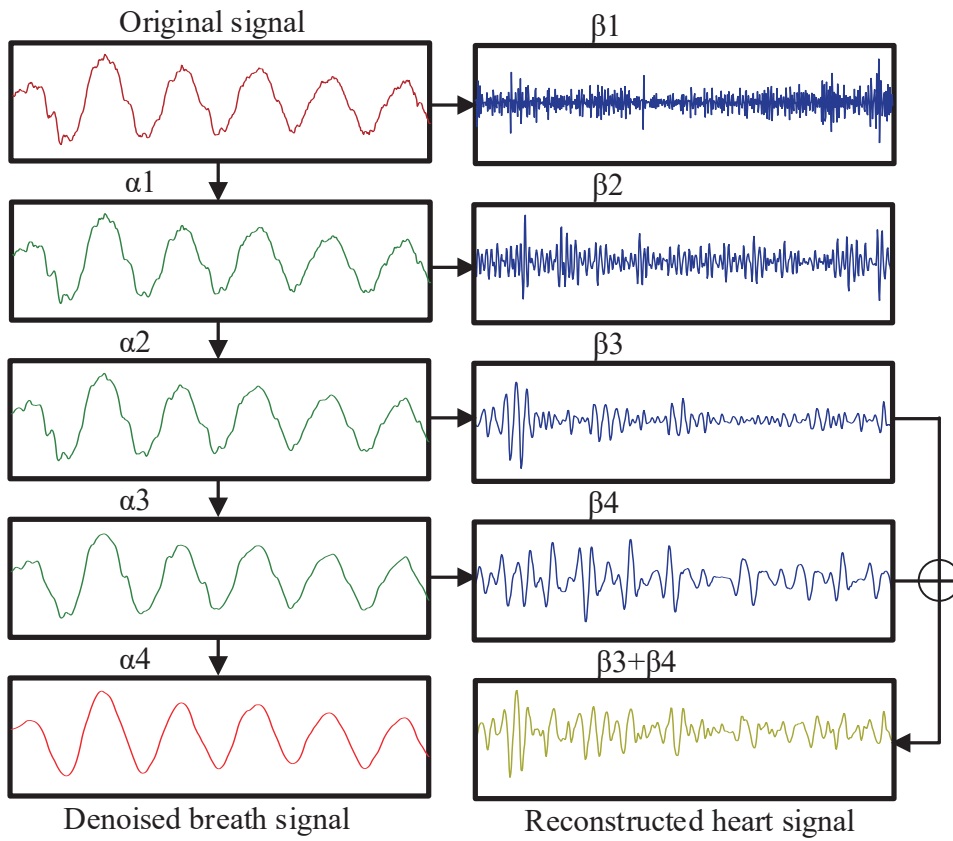
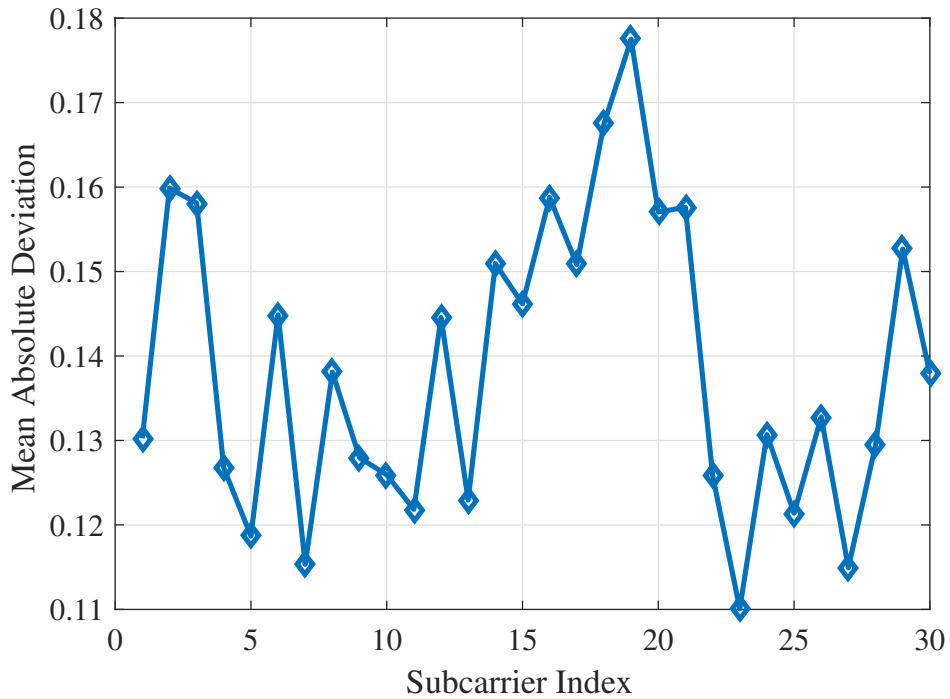Figure 4.5: Discrete wavelet transform results.

Figure 4.6: Mean absolute deviation of each subcarrier.
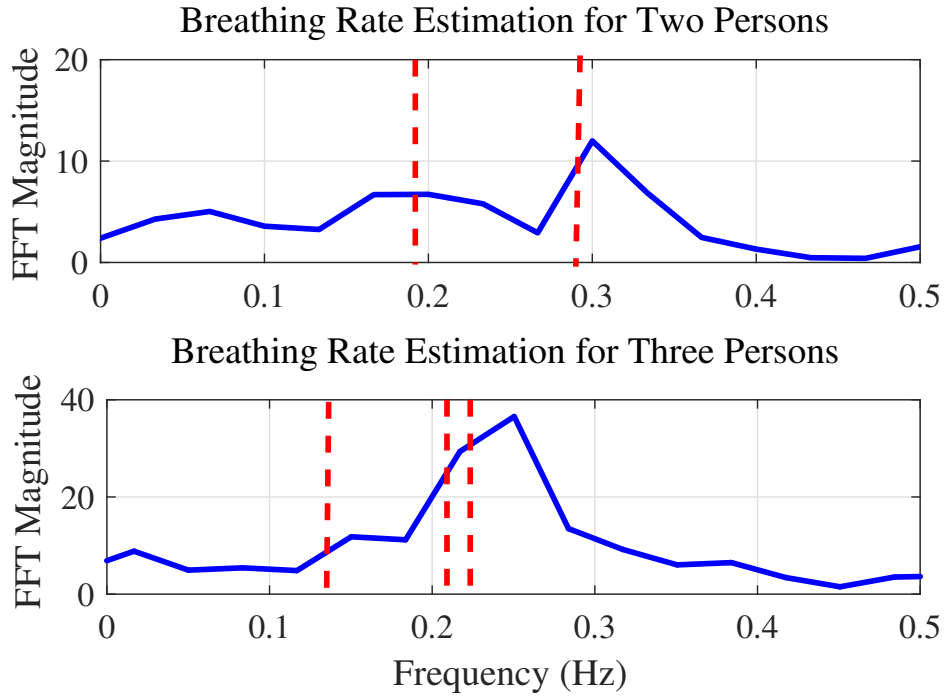
Figure 4.7: Breathing rate estimation for two persons (the upper plot) and three persons (the lower plot) based on FFT.
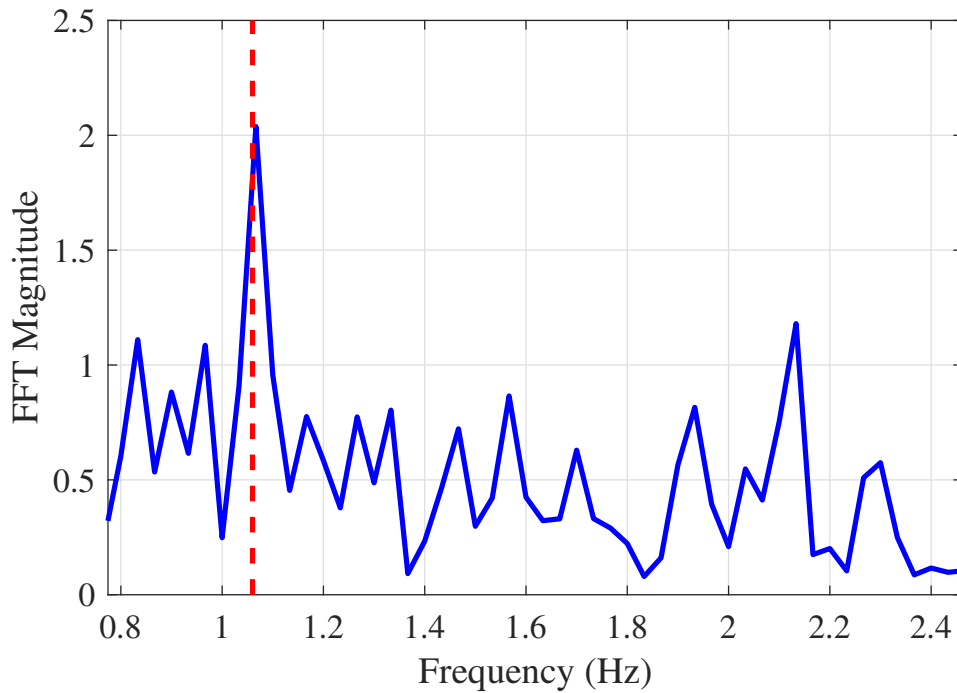

Figure 4.8: Heart rate estimation based on FFT.

becomes larger, the estimation accuracy will be higher, but the larger window size also leads to a lower time domain resolution. Therefore, our PhaseBeat system employs peak detection to estimate the breathing rate based on the approximation coefficient α^L to achieve high accuracy.

However, we find that the approximation coefficient α^L still has fake peaks (i.e., local maximums). We thus use the sliding window method to identify the true peak, where the window size is set to 51 samples based on human's maximum breathing period [13]. Then, we can identify all the peaks by checking whether the median of all the samples in the window is the maximum value or not. After peak detection, all peak-to-peak intervals are averaged to obtain the period of the breathing signal, denoted as P. Finally, the estimated breathing rate can be computed as $60/P$ bpm.

4.3.2 Root-MUSIC for Multiple Person Case

An FFT based method can transform the approximation coefficient α^L from the time domain to the frequency domain to estimate the breathing frequencies for two persons in LOS environments. However, with more persons and more cluttered environments, the FFT based method always leads to poor results, especially when there are two or more breathing rates very close to each other. Fig. 4.7 illustrates the breathing rate estimation for two persons (the upper plot) and three persons (the lower plot) with the FFT method, where the red dotted lines mark the real breathing frequencies (i.e., the ground truth). We can see that the estimated frequencies for the two persons are 0.2 Hz and 0.3 Hz, respectively, which are both quite accurate. However, for the case of three persons, the FFT curve only shows two peaks, and the estimated breathing rates are much less accurate.

To address this issue, we propose a root-MUSIC method to estimate multiple breathing rates based on phase difference data. In fact, we leverage 30 CSI phase difference series patterns after data calibration to build the estimated correlation matrix $\widehat{\mathbf{R}}$, which is given by

$$\widehat{\mathbf{R}} = \mathbf{H}\mathbf{H}^T, \tag{4.4}$$

where $\mathbf{H}$ is a matrix that represents 30 CSI phase difference series after data calibration, which is defined as

$$
\mathbf{H} = \begin{bmatrix} h_1(1) & h_2(1) & \cdots & h_{30}(1) \\ h_1(2) & h_2(2) & \cdots & h_{30}(2) \\ \vdots & \vdots & \cdots & \vdots \\ h_1(I) & h_2(I) & \cdots & h_{30}(I) \end{bmatrix},
\tag{4.5}
$$

where $h_i(j)$ is the phase difference from subcarrier i for packet j after data calibration, and I is the total number of packets. After obtaining the estimated correlation matrix $\mathbf{R}$, we incorporate the standard root-MUSIC method to obtain multiple persons breathing frequencies, which is effective for estimating frequencies of signals consisting of a sum of sinusoids with additive white Gaussian noise [57]. For the same phase difference data for three persons in Fig. 4.7, the breathing frequencies estimated by the proposed method are 0.1467 Hz, 0.2233 Hz, and 0.2483 Hz, respectively, which are much more accurate than those estimated by the FFT based on method. Moreover, we can see that the proposed root-MUSIC method can effectively distinguish two close breathing frequencies.

4.4 Heart Rate Estimation

4.4.1 FFT Based Heart Rate Estimation

Heart rate is an important indicator of health condition and vital sign. Similar to the breathing signal, the heart signal is also periodic, but its magnitude is extremely weak. Usually, breathing signal is orders of magnitude stronger than the heart signal. The movement of the heart (i.e., diastole and systole) only causes small variations in the reflected signal. Moreover, the much stronger breathing signal also generates higher harmonics, which becomes strong interferences to the heart signal. It is thus more challenging to detect the heart rate than the breathing rate.

In PhaseBeat, we employ a directional antenna at the transmitter to improve the power of the reflected signal. Then, the sum of the detail coefficients $\beta^{L-1} + \beta^L$ of the wavelet decomposition is utilized to estimate the heart rate. When the level of decomposition is $L = 4$,

the frequency range is between 0.625 Hz and 2.5 Hz, which filters out the breathing signals, which are between 0.17 Hz and 0.62 Hz, as well as higher frequency noises. Finally, we can use an FFT based method to transform the sum of the detail coefficients $\beta^{L-1} + \beta^L$ to the frequency domain to estimate the heart rate. To improve the frequency resolution, we adopt the method proposed in [5] for heart rate estimation. After finding the peak of FFT, we use the three bins, including the peak bin and its two adjacent bins, where an inverse FFT is performed to obtain a complex time-domain signal. The heart rate is estimated by evaluating the phase of the signal. Fig. 4.8 shows the heart rate estimation with FFT. The PhaseBeat estimated heartbeat frequency is 1.07 Hz, while heartbeat frequency measured by a commercial fingertip pulse sensor is 1.06 Hz. The heart rate estimated error is 0.01 Hz, or 0.6 bpm, in this experiment.

Chapter 5

Experimental Study

5.1 Test Configuration

In this section, we present our extensive experimental study with PhaseBeat in the 5 GHz band. In the experiments, we use a desktop computer as an access point and a Lenovo laptop as a mobile device, both equipped with the Intel 5300 NIC. Our PhaseBeat system is implemented on the Ubuntu desktop 14.04 LTS OS for both the access point and the mobile device. The access point operates in the *monitor mode* and the distance between two adjacent antennas is $d = 2.68$ cm, which is half of the wavelength in the 5 GHz band. The mobile device operates in the *injection mode*, to transmit packets at 400 packets per second using only one antenna. Then, we extract CSI phase difference data between two adjacent antennas at the access point for vital signal estimation.

We conducted extensive experiments with PhaseBeat with four persons over three months. The test scenarios include a computer laboratory and corridors as shown in Fig. 5.1. We have three setups in these two environments for the results reported in this paper. The first setup is within the *laboratory*, a 4.5×8.8 m^2 room. The room is crowed with tables and PCs, which block part of the LOS paths and form a complex radio propagation environment. The second setup is a *through-wall* scenario, where the person is on the transmitter side, separated by a wall from the receiver. The third setup is the 20 m *long corridor*, where the receiver and the transmitter are 11 m apart. We use omnidirectional antennas at both the receiver and transmitter for breathing rate estimation in all the three scenarios. We use a directional antenna at the transmitter in the laboratory scenario for heart rate estimation. For comparison purpose, we
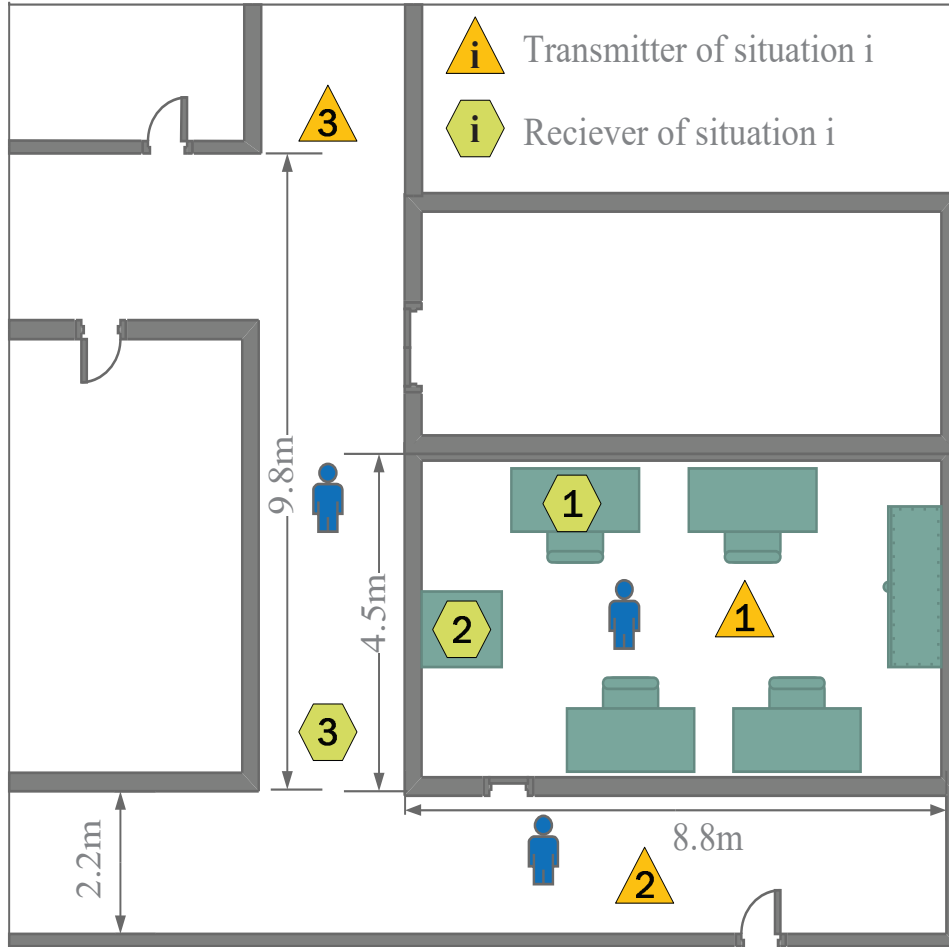
Figure 5.1: Experimental setup scenarios.

employ the NEULOG Respiration Monitor Belt Logger Sensor and a fingertip pulse oximeter to record the ground truths of the breathing and heart rates.

5.2 Performance of Breathing and Heart Rate Estimation

Fig. 5.2 presents the cumulative distribution functions (CDF) of estimation error in breathing rate estimation. We use the amplitude based method [13] as a benchmark in this experiment. We can see that both systems have a similar median estimate error at about 0.25 bpm. However, we can see that for PhaseBeat, 90% of the test data have an estimated error under 0.5 bpm, while 70% of the test data for the amplitude based method have an estimated error under 0.5 bpm. Moreover, the maximum estimation error for PhaseBeat and the amplitude based method are 0.85 bpm and 1.7 bpm, respectively. Therefore, our PhaseBeat system achieves a considerably higher accuracy than the amplitude based method for breathing rate estimation.
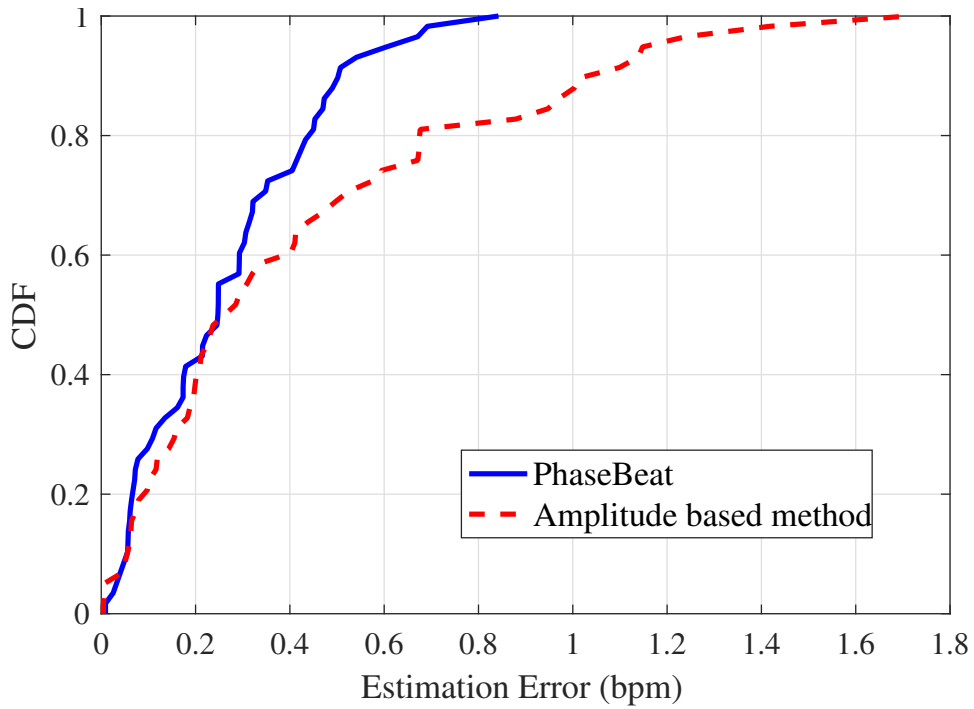
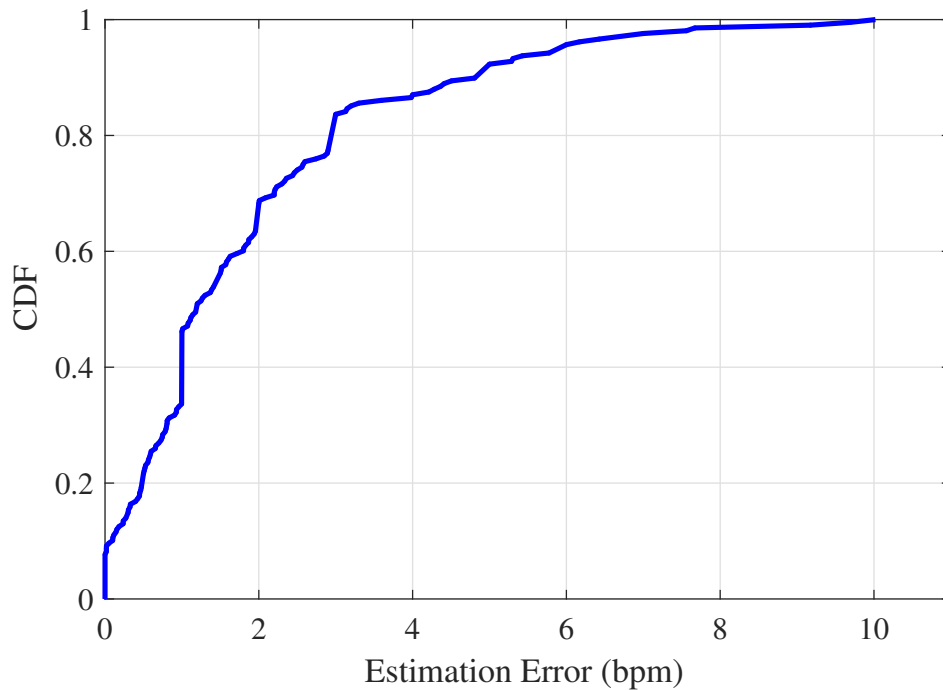Figure 5.2: CDFs of estimation error in breathing rate estimation.

Figure 5.3: CDFs of estimation error in heart rate estimation.

Fig. 5.3 presents the CDF of estimation error in heart rate estimation. For heart signal detection, we need to use the directional antenna at the transmitter to improve the received power. According to Corollary 2.1, we can see that the variation of CSI phase difference data becomes larger, while the variation of CSI amplitude data becomes small, even we cannot
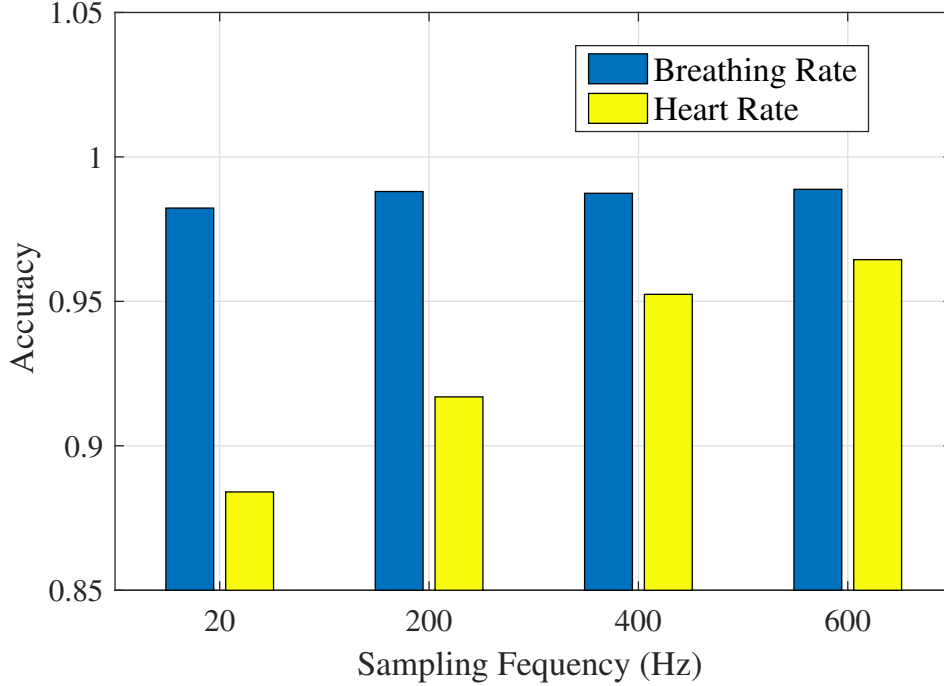
36

Figure 5.4: Accuracy of breathing and heart rates estimation for different sampling frequency.

directly see the periodic heart signal. Thus, we only show the PhaseBeat results for heart signal estimation. In Fig. 5.3, we find that PhaseBeat has a median estimate error of about 1 bpm, while 80% of the test data have an estimated error under 2.5 bpm. Moreover, the maximum estimation error for PhaseBeat is about 10 bpm. We notice that the estimated accuracy of heart rate is lower than the breathing rate estimation because of the much weaker heart signal.

Fig. 5.4 shows the accuracy of breathing and heart rates estimation for different sampling frequencies. For data calibration, we adopt a 400 Hz sampling frequency to estimate the vital signs, which is sufficient to accurately detect the heart signal. As shown in Fig. 5.4, the breathing rate estimation have a similar high accuracy of about 98% for different sampling frequencies. However, the accuracy of the heart rate estimation is only 88% for a sampling frequency of 20 Hz, while it can achieve an accuracy of 95% with the 400 Hz sampling rate. Thus, we choose the 400 Hz sampling rate for PhaseBeat, which is used for all the experimental results in this paper.

Fig. 5.5 shows the accuracy of breathing rates estimation for different numbers of persons. Moreover, we compare the proposed root-MUSIC method using 30 subcarriers with the FFT based method, and with root-MUSIC method using a single subcarrier. It is noticed that for
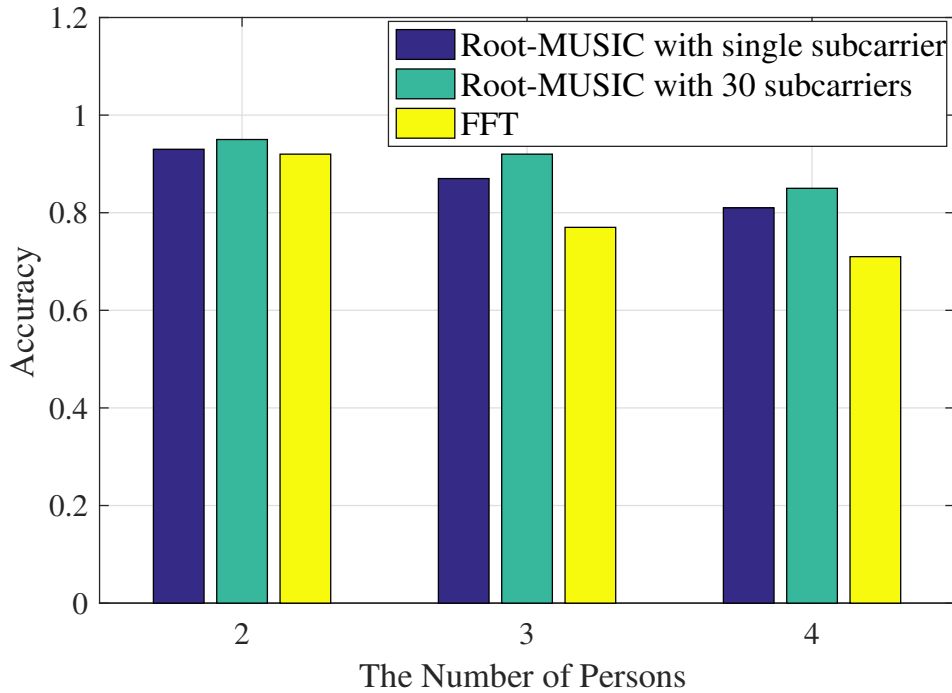
Figure 5.5: Accuracy of breathing rates estimation for different number of persons.

multiple persons, the accuracy of breathing rate estimation decreases for all the three schemes. Moreover, we can see that for two-person breathing rates estimation, the three methods all have a high accuracy above 90%. However, for four persons breathing rate estimation, the root-MUSIC method using 30 subarriers have the best performance among the three.

5.3 Impact of Various Factors

5.3.1 Impact of the Distance between the Transmitter and the Receiver

Fig. 5.6 and Fig. 5.7 show the impact of the distance between the transmitter and the receiver for the long corridor and through-wall scenario, respectively. When the distance between the transmitter and the receiver is increased, the mean estimation error is also increased. This is because the reflected signal is reduced when the distance between the transmitter and receiver is long, which influences the dynamic range of phase difference data. Moreover, we can see that the mean estimation error at the same distance for the through-wall scenario is larger than that for the long corridor scenario. For example, when the distance is 7 m, the mean estimation
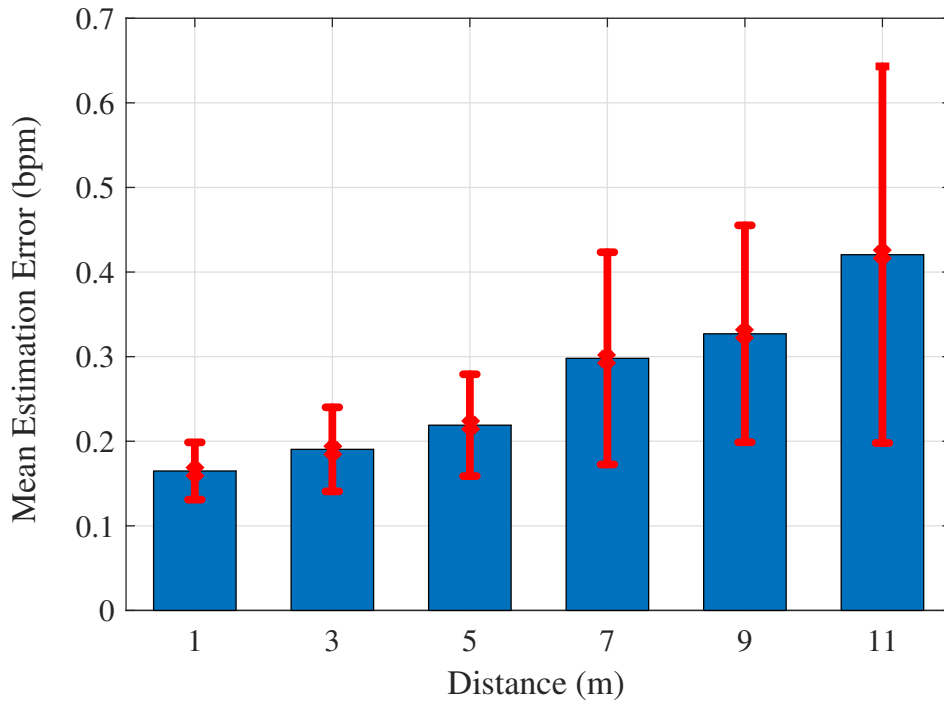
Figure 5.6: Impact of the distance between the transmitter and the receiver for the long corridor.
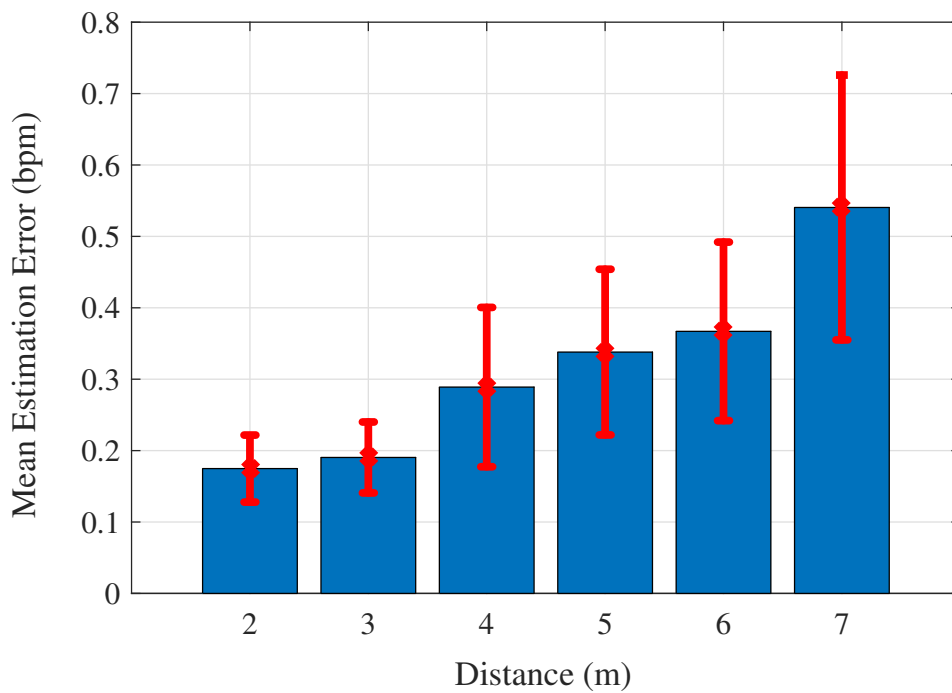

Figure 5.7: Impact of the distance between the transmitter and the receiver for through-wall scenario.

errors for the long corridor and the through-wall scenario are 0.3 bpm and 0.52 bpm, respectively. It is because the signal for the through-wall scenario has a larger attenuation than that for the long corridor scenario.
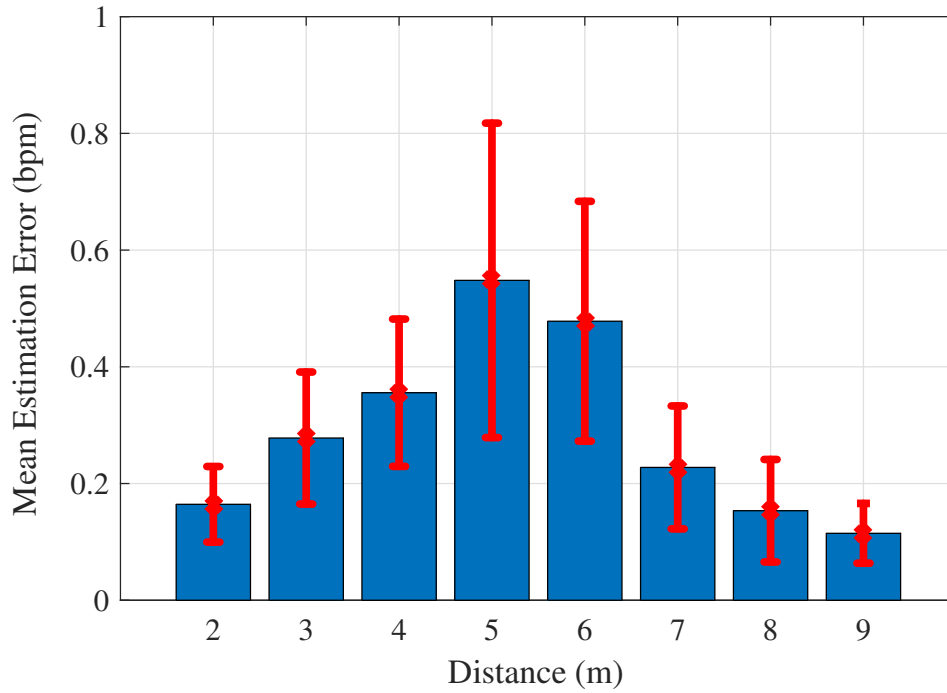
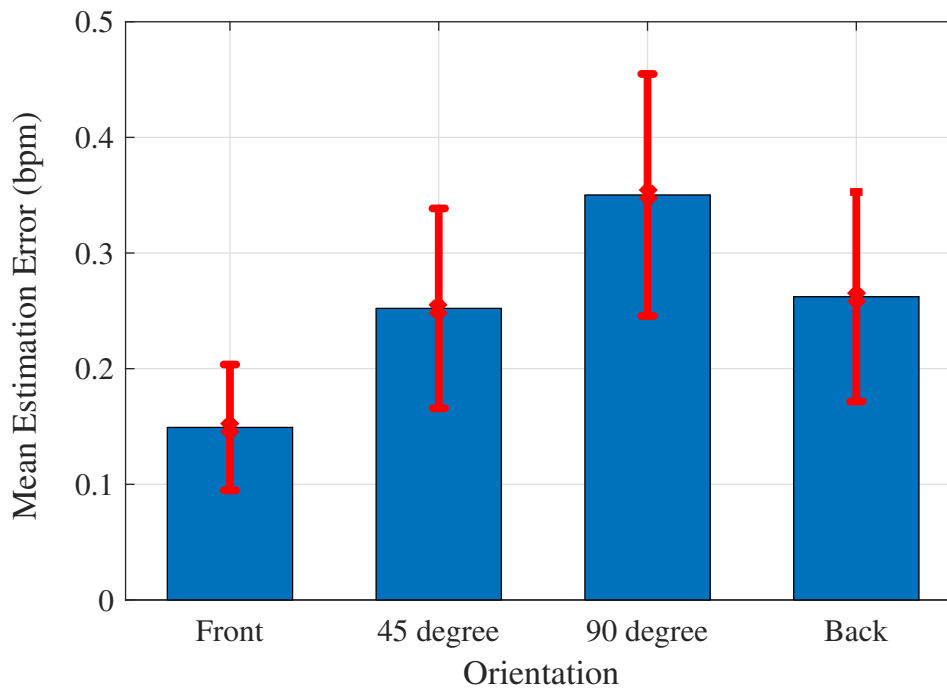Figure 5.8: Impact of the distance between the user and the receiver.

Figure 5.9: Impact of user orientation relative to the receiver.

5.3.2 Impact of the Distance between User and the Receiver

Fig. 5.8 shows the impact of the distance between the user and receiver in the long corridor scenario. We find that when the user locates in the middle of the transmitter and receiver, the
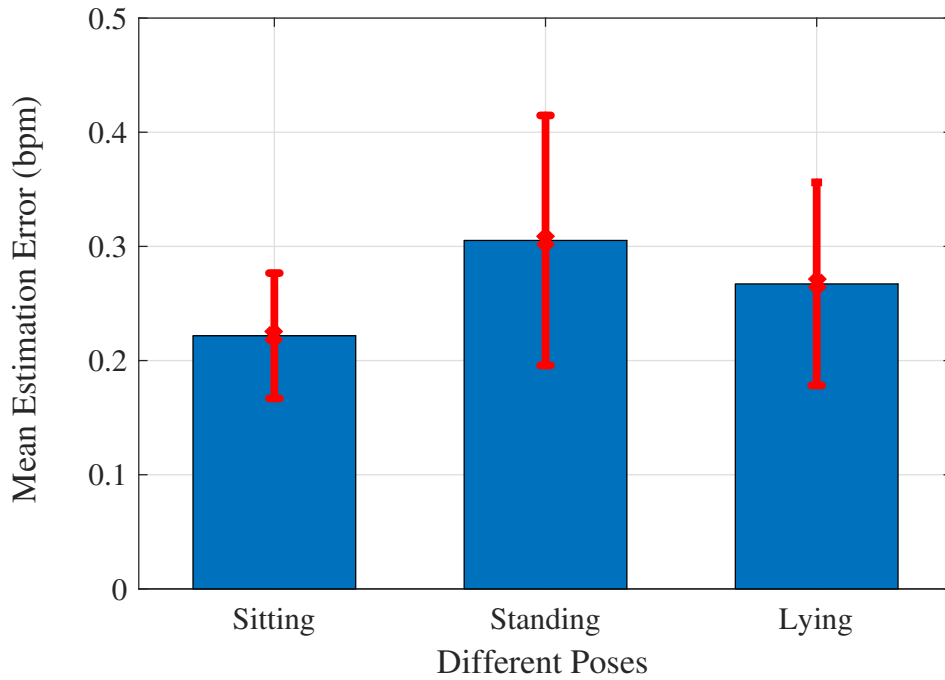
Figure 5.10: Impact of different poses.

mean estimation error is the maximum at about 0.52 bpm. In addition, when the user is close to either the transmitter or the receiver, the estimation error assumes the minimum values at about 0.1 bpm and 0.15 bpm, respectively. When the user is far away with the WiFi devices, the reflected signal from the transmitter is greatly weakened, which influences the usefulness of phase difference data.

5.3.3 Impact of User Orientation Relative to the Receiver

Fig. 5.9 shows the impact of user orientation relative to the receiver in the laboratory environment. We consider four cases including front ($0°$), $45°$, $90°$, and back ($180°$). As shown in Fig. 5.4, the mean estimation error is the maximum at 0.3 bpm at the $90°$ direction. For the front orientation relative to the receiver, we have the minimum error of 0.14 bpm. When the user orientation relative to the receiver is front or back, the reflected component of the wireless signal can effectively capture the chest movements (i.e., inhaling or exhaling). Thus, we can achieve low mean estimation errors in these cases.

5.3.4 Impact of Different Poses

Fig. 5.10 shows the impact of different poses in the laboratory. We consider three common poses for a stationary person such as sitting, standing, and lying. As shown in Fig. 5.10, for the standing pose, the mean estimation error is 0.31 bpm, which is larger than the other poses such as sitting with 0.22 bpm and lying with 0.26 bpm. This is because the chest of the person will have less reflection of the wireless signal when the person is standing.

Chapter 6

Conclusions and Future Work

6.1 Conclusion

In this paper, we presented PhaseBeat, a system that exploits CSI phase difference data to monitor breathing and heartbeats with commodity WiFi device. We first provided a rigorous analysis of CSI phase difference data, with respect to its stability and periodicity. We then described the PhaseBeat design in detail, including environment detection, data calibration, subcarrier selection, and discrete wavelet transform. We implemented PhaseBeat with off-the-shelf WiFi devices, and conducted an extensive experimental study with three setups such as the laboratory, through-wall scenario and the long corridor. The experimental results showed that PhaseBeat can achieve superior performance on breathing and heart rate detection over existing CSI amplitude based methods.

6.2 Future Work

With experiment results, we have already proved that the Phasebeat system is able to monitor the human breathing rate in stable environment. In the future, we also want to expand the system and improve it in the following directions.

6.2.1 Intelligent Disease Precaution System

With the human chest movement monitoring, the Phasebeat system can detect the apnea and other details of the respiration when the user is sleeping. These respiration details can reflect the health condition of the user, and certain apnea can represent the possibility of some special

disease. The intelligent disease precaution system can record the sleeping data and evaluate the user health condition with learning algorithm.

6.2.2 Online Multiple Users Monitoring

With advanced signal processing technique, the system can also separate the breathing signals corresponding to different persons with blind signal separation. However, this kind of technique should need data from a long period of time, and long-time calculation is also necessary. With multiple antennas or other some other devices like RFID tags, the system can separate the different users breathing signals with low calculation time. We plan to extend the system with more devices, so that the system can monitor users respiration data in real-time.

6.2.3 Vital Signs Monitoring in Unstable Environment

Traditionally, RF signal based health monitoring system is very sensitive to the environment. It is very hard to do the vital signs monitoring when the environment is not stable, especially when the user is in moving condition. Large movement will generate large noise in the received signal, which is hard to be separated because the vital signal is usually small signal. In the future, we will propose to make the system can resist the noise coming from user's large body movement.

References

[1] O. Boric-Lubeke and V. Lubecke, "Wireless house calls: using communications technology for health care and monitoring," *IEEE Microwave Mag.*, vol. 3, no. 3, pp. 43–48, 2002.

[2] C. Hunt and F. Hauck, "Sudden infant death syndrome," *Can. Med. Assoc. J*, vol. 174, no. 13, pp. 1309–1310, 2006.

[3] M. L. R. Mogue and B. Rantala, "Capnometers," *Journal of Clinical Monitoring*, 1988.

[4] N. H. Shariati and E. Zahedi, "Comparison of selected parametric models for analysis of the photoplethysmographic signal," in *Proc. 1st IEEE Conf. Comput., Commun. Signal Process.*, Kuala Lumpur, Malaysia, Nov. 2005, pp. 169–172.

[5] F. Adib, H. Mao, Z. Kabelac, D. Katabi, and R. Miller, "Smart homes that monitor breathing and heart rate," in *Proc. ACM CHI'15*, Seoul, Korea, Apr. 2015, pp. 837–846.

[6] A. Droitcour, O. Boric-Lubecke, and G. Kovacs, "Signal-to-noise ratio in doppler radar system for heart and respiratory rate measurements," *IEEE Trans. Microw. Theory Technol.*, vol. 57, no. 10, pp. 2498–2507, Oct. 2009.

[7] P. Nguyen, X. Zhang, A. Halbower, and T. Vu, "Continuous and fine-grained breathing volume monitoring from afar using wireless signals," in *Proc. IEEE INFOCOM'16*, San Francisco, CA, Apr. 2016.

[8] J. Salmi and A. F. Molisch, "Propagation parameter estimation, modeling and measurements for ultrawideband mimo radar," *IEEE Trans. Microw. Theory Technol.*, vol. 59, no. 11, pp. 4257–4267, Nov. 2011.

[9] Z. Yang, P. Pathak, Y. Zeng, X. Liran, and P. Mohapatra, "Monitoring vital signs using millimeter wave," in *Proc. IEEE MobiHoc'16*, Paderborn, Germany, July 2016.

[10] H. Abdelnasser, K. A. Harras, and M. Youssef, "Ubibreathe: A ubiquitous non-invasive wifi-based breathing estimator," in *Proc. IEEE MobiHoc'15*, Hangzhou, China, June 2015, pp. 277–286.

[11] D. Halperin., W. J. Hu., A. Sheth., and D. Wetherall., "Predictable 802.11 packet delivery from wireless channel measurements," in *Proc. ACM SIGCOMM'10*, New Delhi, India, Sept. 2010, pp. 159–170.

[12] Y. Xie, Z. Li, and M. Li, "Precise power delay profiling with commodity wifi," in *Proc. ACM MobiCom'15*, Paris, France, Sept. 2015, pp. 53–64.

[13] J. Liu, Y. Wang, Y. Chen, J. Yang, X. Chen, and J. Cheng, "Tracking vital signs during sleep leveraging off-the-shelf wifi," in *Proc. ACM MobiHoc'15*, Hangzhou, China, June 2015, p. 267276.

[14] D. Hu, S. Mao, and J. H. Reed, "On video multicast in cognitive radio networks," in *INFOCOM 2009, IEEE*. IEEE, 2009, pp. 2222–2230.

[15] M. X. Gong, B. Hart, and S. Mao, "Advanced wireless lan technologies: Ieee 802.11 ac and beyond," *GetMobile: mobile computing and communications*, vol. 18, no. 4, pp. 48–52, 2015.

[16] Y. Xu and S. Mao, "User association in massive mimo hetnets," *IEEE Systems Journal*, vol. 11, no. 1, pp. 7–19, 2017.

[17] M. Feng, S. Mao, and T. Jiang, "Base station ON-OFF switching in 5G wireless systems: Approaches and challenges," *IEEE Wireless Communications*, vol. 24, no. 4, pp. 46–54, Aug. 2017.

[18] ——, "Joint duplex mode selection, channel allocation, and power control for full-duplex cognitive femtocell networks," *Elsevier Digital Communications and Networks Journal*, vol. 1, no. 1, pp. 30–44, Feb. 2015.

[19] M. Feng, T. Jiang, D. Chen, and S. Mao, "Cooperative small cell networks: High capacity for hotspots with interference mitigation," *IEEE Wireless Communications*, vol. 21, no. 6, pp. 108–116, Dec. 2014.

[20] M. Feng, S. Mao, and T. Jiang, "Boost: Base station on-off switching strategy for energy efficient massive mimo hetnets," in *Proc. IEEE INFOCOM 2016*, San Francisco, CA, Apr. 2016, pp. 1395–1403.

[21] X. Wang, "Deployment of high altitude platforms in heterogeneous wireless sensor network via mrf-map and potential games," in *Wireless Communications and Networking Conference (WCNC), 2013 IEEE*. IEEE, 2013, pp. 1446–1451.

[22] K. Xiao, S. Mao, and J. Tugnait, "MAQ: A multiple model predictive congestion control scheme for cognitive radio networks," *IEEE Transactions on Wireless Communications*, vol. 16, no. 4, pp. 2614–2626, Apr. 2017.

[23] ——, "Congestion control for infrastructure-based CRNs: A multiple model predictive control approach," in *Proc. IEEE GLOBECOM 2016*, Washington DC, Dec. 2016, pp. 1–6.

[24] ——, "QoE-driven resource allocation for DASH over OFDMA networks," in *Proc. IEEE GLOBECOM 2016*, Washington, DC, Dec. 2016, pp. 1–6.

[25] Z. He, S. Mao, and S. Kompella, "Quality of experience driven multi-user video streaming in cellular cognitive radio networks with single channel access," *IEEE Transactions on Multimedia*, vol. 18, no. 7, pp. 1401–1413, July 2016.

[26] Z. He, S. Mao, and T. Rappaport, "On link scheduling under blockage and interference in 60 ghz ad hoc networks," *IEEE Access Journal*, vol. 3, pp. 1437–1449, Sept. 2015.

[27] Y. Wang and S. Mao, "On distributed power control in full duplex wireless networks," *Elsevier Digital Communications and Networks Journal*, vol. 3, no. 1, pp. 1–10, Feb. 2017.

[28] N. Tang, S. Mao, Y. Wang, and R. Nelms, "LASSO-based single index model for solar power generation forecasting," in *Proc. IEEE GLOBECOM 2017*, Singapore, Dec. 2017.

[29] Y. Wang, S. Mao, and T. Rappaport, "On directional neighbor discovery in mmwave networks," in *Proc. IEEE ICDCS 2017*, Atlanta, GA, June 2017, pp. 1704–1713.

[30] X. Wang, H. Zhou, S. Mao, S. Pandey, P. Agrawal, and D. Bevly, "Mobility improves LMI-based cooperative indoor localization," in *Proc. IEEE WCNC 2015*, New Orlean, LA, Mar. 2015, pp. 2215–2220.

[31] Z. Jiang and S. Mao, "Energy delay trade-off in multi-channel full-duplex wireless LANs," *IEEE Internet of Things Journal*, vol. 4, no. 3, pp. 658–669, June 2017.

[32] X. Li, T. Jiang, S. Cui, J. An, and Q. Zhang, "Cooperative communications based on rateless network coding in distributed mimo systems [coordinated and distributed mimo]," *IEEE wireless communications*, vol. 17, no. 3, 2010.

[33] J. Gubbi, R. Buyya, S. Marusic, and M. Palaniswami, "Internet of things (iot): A vision, architectural elements, and future directions," *Future generation computer systems*, vol. 29, no. 7, pp. 1645–1660, 2013.

[34] M. Feng and S. Mao, "Interference management and user association for nested array-based massive mimo hetnets," *IEEE Transactions on Vehicular Technology*, 2017.

[35] M. Feng, S. Mao, and T. Jiang, "Boost: Base station on-off switching strategy for grenn massive mimo hetnets," *IEEE Transactions on Wireless Communications*, 2017.

[36] S. R. Islam, D. Kwak, M. H. Kabir, M. Hossain, and K.-S. Kwak, "The internet of things for health care: a comprehensive survey," *IEEE Access*, vol. 3, pp. 678–708, 2015.

[37] Y. Hou, Y. Wang, and Y. Zheng, "Tagbreathe: Monitor breathing with commodity rfid systems," in *Distributed Computing Systems (ICDCS), 2017 IEEE 37th International Conference on*.   IEEE, 2017, pp. 404–413.

[38] F. Adib, H. Mao, Z. Kabelac, D. Katabi, and R. C. Miller, "Smart homes that monitor breathing and heart rate," in *Proceedings of the 33rd annual ACM conference on human factors in computing systems.* ACM, 2015, pp. 837–846.

[39] X. Wang, R. Huang, and S. Mao, "Sonarbeat: Sonar phase for breathing beat monitoring with smartphones," in *Proc. ICCCN 2017*, Vancouver, Canada, July/Aug. 2017, pp. 1–8.

[40] ——, "Demo abstract: Sonarbeat: Sonar phase for breathing beat monitoring with smartphones," in *Proc. IEEE SECON 2017*, San Diego, CA, June 2017, pp. 1–2.

[41] L. Tarassenko, M. Villarroel, A. Guazzi, J. Jorge, D. Clifton, and C. Pugh, "Non-contact video-based vital sign monitoring using ambient light and auto-regressive models," *Physiological measurement*, vol. 35, no. 5, p. 807, 2014.

[42] H. Aly and M. Youssef, "Zephyr: Ubiquitous accurate multi-sensor fusion-based respiratory rate estimation using smartphones," in *Proc. IEEE INFOCOM'16*, San Francisco, CA, Apr. 2016, pp. 1–9.

[43] J. Liu, Y. Wang, Y. Chen, J. Yang, X. Chen, and J. Cheng, "Tracking vital signs during sleep leveraging off-the-shelf wifi," in *Proceedings of the 16th ACM International Symposium on Mobile Ad Hoc Networking and Computing.* ACM, 2015, pp. 267–276.

[44] Z. Yang, Z. Zhou, and Y. Liu, "From RSSI to CSI: Indoor localization via channel response," *ACM Comput. Surv.*, vol. 46, no. 2, Nov. 2013.

[45] X. Wang, C. Yang, and S. Mao, "ResBeat: Resilient breathing beats monitoring with online bimodal CSI data," in *Proc. IEEE GLOBECOM 2017*, Singapore, Dec. 2017.

[46] C. G. Scully, J. Lee, J. Meyer, A. M. Gorbach, D. Granquist-Fraser, Y. Mendelson, and K. H. Chon, "Physiological parameter monitoring from optical recordings with a mobile phone," *IEEE Transactions on Biomedical Engineering*, vol. 59, no. 2, pp. 303–306, 2012.

[47] P. Ray, "A survey on internet of things architectures," *Journal of King Saud University-Computer and Information Sciences*, 2016.

[48] X. Wang, L. Gao, S. Mao, and S. Pandey, "Csi-based fingerprinting for indoor localization: A deep learning approach," *IEEE Transactions on Vehicular Technology*, vol. 66, no. 1, pp. 763–776, 2017.

[49] X. Wang, X. Wang, and S. Mao, "Resloc: Deep residual sharing learning for indoor localization with csi tensors," in *Proc. IEEE PIMRC 2017*, Montreal, Canada, Oct. 2017.

[50] J. Xiong and K. Jamieson, "Arraytrack: A fine-grained indoor location system," in *Proc. ACM NSDI'13*, Lombard. IL, Apr. 2013, pp. 71–84.

[51] M. Speth, S. Fechtel, G. Fock, and H. Meyr, "Optimum receiver design for wireless broadband systems using OFDM–Part I," *IEEE Trans. Commun.*, vol. 47, no. 11, pp. 1668–1677, Nov. 1999.

[52] X. Wang, C. Yang, and S. Mao, "Tensorbeat: Tensor decomposition for monitoring multi-person breathing beats with commodity WiFi," *ACM Transactions on Intelligent Systems and Technology*, vol. 9, no. 1, pp. 8:1–8:27, Sept. 2017.

[53] X. Wang, L. Gao, and S. Mao, "Biloc: Bi-modal deep learning for indoor localization with commodity 5ghz wifi," *IEEE Access*, vol. 5, pp. 4209–4220, 2017.

[54] X. Wang, X. Wang, and S. Mao, "Cifi: Deep convolutional neural networks for indoor localization with 5 ghz wi-fi," in *Communications (ICC), 2017 IEEE International Conference on*. IEEE, 2017, pp. 1–6.

[55] J. Gjengset, J. Xiong, G. McPhillips, and K. Jamieson, "Phaser: Enabling phased array signal processing on commodity WiFi access points," in *Proc. ACM MobiCom'14*, Maui, HI, Sept. 2014, pp. 153–164.

[56] S. Sardy, P. Tseng, and A. Brace, "Robust wavelet denoising," *IEEE Trans. Signal Process.*, vol. 49, no. 6, pp. 1146–1152, Jun. 2001.

[57] B. D. Rao and K. V. S. Hari, "Performance analysis of root-music," *IEEE Trans. Acoust., Speech, Signal Process.*, vol. 37, no. 12, pp. 1939–1949, Dec. 1989.